

Journal of
**Applied
Crystallography**
ISSN 0021-8898
Editor: **Gernot Kostorz**

Exploratory orientation data analysis with ω sections

K. Gerald van den Boogaart and Helmut Schaeben

Copyright © International Union of Crystallography

Author(s) of this paper may load this reprint on their own web site provided that this cover page is retained. Republication of this article or its storage in electronic databases or the like is not permitted without prior permission in writing from the IUCr.

Exploratory orientation data analysis with ω sections

K. Gerald van den Boogaart^{a*} and Helmut Schaeben^b

Received 18 September 2003

Accepted 11 May 2004

^aDepartment of Mathematics and Computer Science, Ernst-Moritz-Arndt-Universität Greifswald, Institut f48, 17489 Greifswald, Germany, and ^bGeoscience Mathematics and Informatics, Freiberg University of Mining and Technology, Freiberg, Germany. Correspondence e-mail: gerald.boogaart@uni-greifswald.de

Since the domain of crystallographic orientations is three-dimensional and spherical, insightful visualization of them or visualization of related probability density functions requires (i) exploitation of the effect of a given orientation on the crystallographic axes, (ii) consideration of spherical means of the orientation probability density function, in particular with respect to one-dimensional totally geodesic submanifolds, and (iii) application of projections from the two-dimensional unit sphere $S^2 \subset \mathbb{R}^3$ onto the unit disk $D \subset \mathbb{R}^2$. The familiar crystallographic ‘pole figures’ are actually mean values of the spherical Radon \mathcal{R}_1 transform. The mathematical Radon \mathcal{R}_1 transform associates a real-valued function f defined on a sphere with its mean values $\mathcal{R}_1 f$ along one-dimensional circles with centre \mathcal{O} , the origin of the coordinate system, and spanned by two unit vectors. The family of views suggested here defines ω sections in terms of simultaneous orientational relationships of two different crystal axes with two different specimen directions, such that their superposition yields a user-specified pole probability density function. Thus, the spherical averaging and the spherical projection onto the unit disk determine the distortion of the display. Commonly, spherical projections preserving either volume or angle are favoured. This rich family displays f completely, *i.e.* if f is given or can be determined unambiguously, then it is uniquely represented by several subsets of these views. A computer code enables the user to specify and control interactively the display of linked views, which is comprehensible as the user is in control of the display.

© 2004 International Union of Crystallography
Printed in Great Britain – all rights reserved

1. Introduction

A crystallographic orientation is the active rotation $\mathbf{g} \in SO(3)$ which maps a right-handed coordinate system K_S fixed to the specimen onto another right-handed coordinate system K_C fixed to the crystal:

$$K_C = \mathbf{g} K_S. \quad (1)$$

It may be parameterized by three conventionally defined Euler angles, *e.g.* $\mathbf{g} \in G \subset SO(3)$: $\mathbf{g} = g(\alpha, \beta, \gamma)$, where the first rotation by $\alpha \in [0, 2\pi)$ is about the \mathbf{z}_{K_S} axis, the second by $\beta \in [0, \pi]$ about the new \mathbf{y}' axis, and the third by $\gamma \in [0, 2\pi)$ about the new \mathbf{z}'' axis of the specimen coordinate system K_S . Then (α, β) are the spherical coordinates of the direction $\mathbf{z}'' = \mathbf{z}_{K_C}$ with respect to K_S (*cf.* Matthies *et al.*, 1987). This sequence of rotations results in the same orientation as the sequence of the first rotation by $\gamma \in [0, 2\pi)$ about the \mathbf{z}_{K_S} axis, the second by $\beta \in [0, \pi]$ about the (old) \mathbf{y}_{K_S} axis, the third by $\alpha \in [0, 2\pi)$ about the (old) \mathbf{z}_{K_S} axis of the specimen coordinate system K_S , as can be seen by multiple applications of conjugation of rotations:

$$\begin{aligned} M(\alpha; \mathbf{z}) M(\beta; \mathbf{y}) M(\gamma; \mathbf{z}) &= \underbrace{M(\alpha; \mathbf{z}) M(\beta; \mathbf{y}) M^{-1}(\alpha; \mathbf{z})}_{M(\beta; [M(\alpha; \mathbf{z}) \mathbf{y}])} \underbrace{M(\alpha; \mathbf{z}) M(\gamma; \mathbf{z}) M^{-1}(\alpha; \mathbf{z})}_{M(\gamma; \mathbf{z})} \\ &\times M(\alpha; \mathbf{z}) \\ &= \underbrace{M(\beta; \mathbf{y}') M(\gamma; \mathbf{z}) M^{-1}(\beta; \mathbf{y}')}_{M(\gamma; [M(\beta; \mathbf{y}') \mathbf{z}])} M(\beta; \mathbf{y}') M(\alpha; \mathbf{z}) \\ &= M(\gamma; \mathbf{z}'') M(\beta; \mathbf{y}') M(\alpha; \mathbf{z}). \end{aligned} \quad (2)$$

Essentially, there exist 11 other ways to define Euler angles, *e.g.* Bunge’s $(\varphi_1, \Phi, \varphi_2)$, and they are all in use (Kuipers, 1999).

The coordinates of a unique direction denoted \mathbf{h}_{K_C} with respect to the crystallographic coordinate system $K_C = \mathbf{g} K_S$ and \mathbf{r}_{K_S} with respect to the specimen coordinate system K_S are related to each other by

$$\mathbf{h}_{K_C} = \mathbf{g}^{-1} \mathbf{r}_{K_S}, \quad (3)$$

where \mathbf{g}^{-1} is represented by the matrix

$$M[\mathbf{g}^{-1}(\alpha, \beta, \gamma)]$$

$$\begin{aligned}
 &= \left[\begin{pmatrix} \cos \alpha & -\sin \alpha & 0 \\ \sin \alpha & \cos \alpha & 0 \\ 0 & 0 & 1 \end{pmatrix} \begin{pmatrix} \cos \beta & 0 & \sin \beta \\ 0 & 1 & 0 \\ -\sin \beta & 0 & \cos \beta \end{pmatrix} \right. \\
 &\quad \left. \times \begin{pmatrix} \cos \gamma & -\sin \gamma & 0 \\ \sin \gamma & \cos \gamma & 0 \\ 0 & 0 & 1 \end{pmatrix} \right]^{-1} \\
 &= \begin{pmatrix} \cos \gamma & \sin \gamma & 0 \\ -\sin \gamma & \cos \gamma & 0 \\ 0 & 0 & 1 \end{pmatrix} \begin{pmatrix} \cos \beta & 0 & -\sin \beta \\ 0 & 1 & 0 \\ -\sin \beta & 0 & \cos \beta \end{pmatrix} \\
 &\quad \times \begin{pmatrix} \cos \alpha & \sin \alpha & 0 \\ -\sin \alpha & \cos \alpha & 0 \\ 0 & 0 & 1 \end{pmatrix} \\
 &= \begin{pmatrix} \cos \alpha \cos \beta \cos \gamma & \sin \alpha \cos \beta \cos \gamma & -\sin \beta \cos \gamma \\ -\sin \alpha \sin \gamma & +\cos \alpha \sin \gamma & \\ -\cos \alpha \cos \beta \sin \gamma & -\sin \alpha \cos \beta \sin \gamma & \sin \beta \sin \gamma \\ -\sin \alpha \cos \gamma & +\cos \alpha \cos \gamma & \\ \cos \alpha \sin \beta & \sin \alpha \sin \beta & \cos \beta \end{pmatrix} \\
 &= M'[\mathbf{g}(\alpha, \beta, \gamma)].
 \end{aligned}$$

It should be noted that the commonly applied convention in texture analysis following the most influential books on texture analysis by Bunge (1969, 1982) is to – in a strict mathematical sense incorrectly – refer to both the active rotation \mathbf{g} of coordinate systems $\mathbf{g}K_S = K_C$ and the passive transformation $g = \mathbf{g}^{-1}$ of unit vectors $\mathbf{h}_{K_C} = \mathbf{g}^{-1}\mathbf{r}_{K_S}$ by the unique symbol g . Since it is essential to work with (3) rather than (1), formal consistency of the formulae given here with respect to previous references could be maintained by identifying $\mathbf{g} = g^{-1}$, and *vice versa*.

Since the domain of crystallographic orientations is three-dimensional and spherical, insightful visualization of them or visualization of related probability density functions requires (i) exploitation of the effect of a given orientation on several crystallographic axes simultaneously, (ii) consideration of spherical pole probability density functions augmented with information concerning the orientational relationship of an additional crystallographic and an additional specimen direction, and (iii) application of appropriate projections from the two-dimensional unit sphere $S^2 \subset \mathbb{R}^3$ onto the unit disk $D \subset \mathcal{R}^E$.

2. Motivation of ω sections of the orientation space

Conventionally, the information conveyed by orientation data or their orientation probability density function is visualized

by point plots or plots of contour lines of equal density in two-dimensional sections of the orientation space along one of the Euler angles, *i.e.* in sections orthogonal to a coordinate axis of the Euler space, thought of as being spanned by three orthogonal axes. Displayed in this fashion, plots of the orientation space and its sections suffer from serious distortions (*cf.* Kunze, 1991; Kocks *et al.*, 1999); since distances and angles are generally not preserved, the visual inspection, especially the interpretation of local maxima, may be misleading. More involved are pole-figure-like plots of orientation probability density functions in γ sections (Wenk & Kocks, 1987) of the Euler space along constant values of γ , and particularly in σ sections (Helming *et al.*, 1988; Matthies *et al.*, 1990*a,b*; Kunze, 1991) or δ sections, respectively, which display orientation probability density functions according to the parametrization $\mathbf{g} = \mathbf{g}(\alpha, \beta, \sigma)$ of an orientation with $\sigma = (\alpha + \gamma)/2$ to avoid the effects of the singularity of the parametrization $\mathbf{g}(\alpha, \beta, \gamma)$ for $\beta = 0$, or analogously according to the parametrization $\mathbf{g} = \mathbf{g}(\delta, \beta, \gamma)$ with $\delta = (\alpha - \gamma)/2$ to avoid the effect of the $\beta = \pi$ singularity of the parametrization $\mathbf{g}(\alpha, \beta, \gamma)$. σ sections preserve and display equal-volume portions of the orientation space, and present a good compromise to preserve distances and angles. Like γ sections, they add up to the \mathbf{z}_{K_C} -pole probability density plot, or the \mathbf{z}_{K_S} -inverse-pole probability density plot, but other axes or their statistical distributions, respectively, are not visually inferred.

γ sections exploit the fact that for arbitrary Euler angles $\alpha, \beta, \mathbf{g}(\alpha, \beta, \gamma)$ rotates the crystal direction $\mathbf{h} = \mathbf{z}_{K_C} = (0, 0, 1)^t$ onto $\mathbf{r} = (\cos \alpha \sin \beta, \sin \alpha \sin \beta, \cos \beta)^t$ for each $\gamma \in [0, 2\pi)$, *i.e.* $\mathbf{g}(\alpha, \beta, \gamma)\mathbf{z}_{K_C} = \mathbf{r}$ for each $\gamma \in [0, 2\pi)$, where γ refers, according to (2), to a rotation about $\mathbf{z}'' = \mathbf{g}(\alpha, \beta, 0)\mathbf{z}_{K_C} = \mathbf{r}$. The rotation angle γ is also the orientation distance of $\mathbf{g}(\alpha, \beta, \gamma)$ and the reference orientation $\mathbf{g}(\alpha, \beta, 0)$ as $\mathbf{g}(\alpha, \beta, \gamma)\mathbf{g}^{-1}(\alpha, \beta, 0)$ results in a rotation by γ about \mathbf{r} .

The idea to visualize orientation data and their probability density function in sections of the orientation space is generalized by the definition of the ω section in terms of a simultaneous visualization of orientational relationships of two pairs of one crystallographic and one specimen direction each, as initially introduced by Schaeben & Boogaart (2002, 2003). More specifically, we generalize the idea of γ sections for arbitrary crystal directions \mathbf{h} and an orientation distance generally denoted ω given in terms of an additional crystal direction \mathbf{h}_1 and an additional specimen direction \mathbf{v} . For each direction $\mathbf{r} = \mathbf{g}\mathbf{h}$, the angle $\omega(\mathbf{r})$ is the specific orientation distance between the actual orientation \mathbf{g} mapping \mathbf{h} onto \mathbf{r} and a reference orientation \mathbf{g}_0 mapping both \mathbf{h} onto \mathbf{r} and simultaneously \mathbf{h}_1 onto \mathbf{v} . Since an orientation distance is always a rotation angle of some rotation, we have characterized this rotation as a rotation about $\mathbf{r} = \mathbf{g}\mathbf{h}$.

3. Individual crystallographic orientation measurements

The data set consists of crystallographic orientations $\mathbf{g}_i \in SO(3)$, $i = 1, \dots, n$, where n denotes the total number of orientation measurements, *i.e.* the sample size. The corre-

sponding \mathbf{h} -pole point plot displays the projection of the unit vectors $\mathbf{g}_i \mathbf{h}_k = \mathbf{r}_{i_k} \in S^2, i = 1, \dots, n, k = 1, \dots, m(\mathbf{h})$, onto the unit disk D , where $m(\mathbf{h})$ denotes the crystallographic multiplicity of the crystal direction \mathbf{h} due to crystallographic symmetry. Thus, an orientation \mathbf{g}_i is displayed at the location $\mathbf{r}_i = \mathbf{g}_i \mathbf{h}$ and at all locations corresponding to crystal-symmetry-equivalent directions \mathbf{h}_k of \mathbf{h} when appropriately projected onto the unit disk. Due to crystal geometry, this representation of \mathbf{g}_i by the points $\mathbf{r}_{i_k} = \mathbf{g}_i \mathbf{h}_k$ is in general complete, if the crystallographic multiplicity $m(\mathbf{h}) > 1$. It is incomplete in the case of triclinic symmetry ('no symmetry'), for \mathbf{c} -pole point plots in the case of non-cubic symmetries, or for pole probability density plots, which display integral ('summary') information about the orientations, blurring the crystal geometrical relationships.

Neglecting crystallographic symmetry and dropping the subscript k momentarily, the existence of a point \mathbf{r}_i in the \mathbf{h} -pole point plot provides the information that there is at least one orientation \mathbf{g}_i in the sample with $\mathbf{g}_i \mathbf{h} = \mathbf{r}_i$. However, the two directions, *i.e.* the crystallographic direction \mathbf{h} and the specimen direction \mathbf{r}_i , do not uniquely define an orientation. In fact, the set $G(\mathbf{h}, \mathbf{r}_i) \subset SO(3)$ of rotations with $\mathbf{g} \mathbf{h} = \mathbf{r}_i$ constitutes a circle in $S^3 \subset \mathbb{R}^4$ with centre \mathcal{O} if the orientations are represented by quaternions (Schaeben, 1996). The elements of $G(\mathbf{h}, \mathbf{r}_i)$ can be decomposed into a sequence of three successive rotations in different ways, *e.g.* by

$$\mathbf{g} \mathbf{h} = \mathbf{g}'_3 \mathbf{g}'_2 \underbrace{\mathbf{g}'_1 \mathbf{h}}_{\mathbf{z}} = \mathbf{g}'_3 \underbrace{\mathbf{g}'_2 \mathbf{z}}_{\mathbf{z}} = \mathbf{g}'_3 \mathbf{z} = \mathbf{r}_i,$$

where $\mathbf{g}'_3 \mathbf{z} = \mathbf{r}_i$ and $\mathbf{g}'_1 \mathbf{h} = \mathbf{z}$ are specified rotations, and $\mathbf{g}'_2 \mathbf{z} = \mathbf{z}$ is any rotation about \mathbf{z} by a variable angle (*cf.* Matthies *et al.*, 1987), or as well by

$$\mathbf{g} \mathbf{h} = \mathbf{g}_3 \mathbf{g}_2 \underbrace{\mathbf{g}_1 \mathbf{h}}_{\mathbf{h}} = \mathbf{g}_3 \underbrace{\mathbf{g}_2 \mathbf{h}}_{\mathbf{z}} = \mathbf{g}_3 \mathbf{z} = \mathbf{r}_i,$$

and, equivalently,

$$\mathbf{g} \mathbf{h} = \mathbf{g}_4 \mathbf{g}_3 \underbrace{\mathbf{g}_2 \mathbf{h}}_{\mathbf{z}} = \mathbf{g}_4 \underbrace{\mathbf{g}_3 \mathbf{z}}_{\mathbf{r}_i} = \mathbf{g}_4 \mathbf{r}_i = \mathbf{r}_i, \quad (4)$$

where $\mathbf{g}_3 \mathbf{z} = \mathbf{r}_i$ and $\mathbf{g}_2 \mathbf{h} = \mathbf{z}$ are specified rotations $\mathbf{g}_3(\varphi, \vartheta) \mathbf{g}_2(\alpha, \beta) =: \mathbf{g}_0(\alpha, \beta; \varphi, \vartheta)$ such that $\mathbf{g}_3 \mathbf{g}_2 \mathbf{h} = \mathbf{g}_0 \mathbf{h} = \mathbf{r}$, and $\mathbf{g}_1 \mathbf{h} = \mathbf{h}$ is any rotation about \mathbf{h} by a variable angle of rotation, and $\mathbf{g}_4 \mathbf{r}_i = \mathbf{r}_i$ is any rotation about \mathbf{r}_i by a variable angle of rotation. Accordingly, the set $G(\mathbf{h}, \mathbf{r}) = \{\mathbf{g} \in SO(3) \mid \mathbf{g} \mathbf{h} = \mathbf{r}\}$ of all rotations with $\mathbf{g} \mathbf{h} = \mathbf{r}$ may be represented by matrices $M(\mathbf{g}; \mathbf{h}, \mathbf{r}) \in SO(3)$ in terms of Euler angles as

$$M(\mathbf{g}; \mathbf{h}, \mathbf{r}) = \underbrace{M(\varphi, \vartheta, 0)}_{\mathbf{z} \mapsto \mathbf{r}} \underbrace{M(0, 0, \omega)}_{\mathbf{z} \mapsto \mathbf{z}} \underbrace{M^{-1}(\alpha, \beta, 0)}_{\mathbf{h} \mapsto \mathbf{z}} \quad (5)$$

$$= M(\varphi, \vartheta, 0) M(\omega; \mathbf{z}) M'(\alpha, \beta, 0) \quad (6)$$

with

$$M'(\alpha, \beta, 0) = \begin{pmatrix} \cos \alpha \cos \beta & \sin \alpha \cos \beta & -\sin \beta \\ -\sin \alpha & \cos \alpha & 0 \\ \cos \alpha \sin \beta & \sin \alpha \sin \beta & \cos \beta \end{pmatrix},$$

where α, β are the spherical coordinates of \mathbf{h} ,

$$M(\varphi, \vartheta, 0) = \begin{pmatrix} \cos \varphi \cos \vartheta & -\sin \varphi & \cos \varphi \sin \vartheta \\ \sin \varphi \cos \vartheta & \cos \varphi & \sin \varphi \sin \vartheta \\ -\sin \vartheta & 0 & \cos \vartheta \end{pmatrix},$$

where φ, ϑ are the spherical coordinates of \mathbf{r} , and

$$M(0, 0, \omega) = \begin{pmatrix} \cos \omega & -\sin \omega & 0 \\ \sin \omega & \cos \omega & 0 \\ 0 & 0 & 1 \end{pmatrix} = M(\omega; \mathbf{z}).$$

Since it holds that

$$\begin{aligned} M(\omega; \mathbf{z}) &= M'(\varphi, \vartheta, 0) M[\omega; M(\varphi, \vartheta, 0) \mathbf{z} M(\varphi, \vartheta, 0)] \\ &= M'(\alpha, \beta, 0) M[\omega; M(\alpha, \beta, 0) \mathbf{z}] M(\alpha, \beta, 0), \end{aligned} \quad (7)$$

then

$$\begin{aligned} M(\mathbf{g}; \mathbf{h}, \mathbf{r}) &= M[\omega; M(\varphi, \vartheta, 0) \mathbf{z}] M(\varphi, \vartheta, 0) M'(\alpha, \beta, 0) \\ &= M(\omega; \mathbf{r}) M(\varphi, \vartheta, 0) M'(\alpha, \beta, 0) \\ &= M(\omega; \mathbf{r}) M(\alpha, \beta, \varphi, \vartheta), \end{aligned} \quad (8)$$

where $M(\alpha, \beta, \varphi, \vartheta)$ is a rotation matrix specified by the four involved spherical coordinates. Obviously, any matrix M' with $M' \mathbf{h} = \mathbf{r}$ will also suffice. Thus, $\omega \in [0, 2\pi)$ provides a degree of freedom, of choice, which will be of importance later on.

Analogously, of course,

$$\begin{aligned} M(\mathbf{g}; \mathbf{h}, \mathbf{r}) &= M(\varphi, \vartheta, 0) M'(\alpha, \beta, 0) M(\omega; \mathbf{h}) \\ &= M(\alpha, \beta, \varphi, \vartheta) M(\omega; \mathbf{h}). \end{aligned} \quad (9)$$

Thus, for a data set $\{\mathbf{g}_i \in SO(3)\}$ with $\mathbf{g}_i \mathbf{h} = \mathbf{r}_i$, the elements of $G(\mathbf{h}, \mathbf{r}_i)$ may be thought of as differing by an initial rotation about \mathbf{h} , or a final rotation about \mathbf{r}_i , respectively, by an arbitrary angle $\omega \in [0, 2\pi)$. The actual ω can be determined when the effect of \mathbf{g}_i on another crystallographic direction \mathbf{h}_1 is considered by additionally plotting in each point $\mathbf{r}_i = \mathbf{g}_i \mathbf{h}$ the projection of $\mathbf{g}_i \mathbf{h}_1$ onto the tangential plane at \mathbf{r}_i . Since an orientation can be uniquely determined by two pairs of directions, each of which consists of one crystallographic and one specimen direction (*cf.* Altmann, 1986; Bukharova, 1996), the orientation is even more instructively uniquely determined if the angle ω relates the crystallographic direction \mathbf{h}_1 , strictly speaking $\mathbf{g}_i \mathbf{h}_1$, to another specimen direction \mathbf{v} provided that $\mathbf{v} \neq \mathbf{r}_i$, *i.e.* if ω is the angle enclosed by the orthogonal projection $(\mathbf{g}_i \mathbf{h}_1)_T(\mathbf{r}_i)$ of $\mathbf{g}_i \mathbf{h}_1$ and the orthogonal projection $(\mathbf{v})_T(\mathbf{r}_i)$ of a second user-defined specimen direction \mathbf{v} onto the tangential plane at \mathbf{r}_i when looking at the tangential plane from outside the pole sphere, *i.e.* for $\mathbf{v} \neq \mathbf{r}_i$, by

$$\omega(\mathbf{r}_i) := \angle[(\mathbf{v})_T(\mathbf{r}_i), (\mathbf{g}_i \mathbf{h}_1)_T(\mathbf{r}_i)] \quad (10)$$

with

$$(\mathbf{v})_T(\mathbf{r}_i) := \mathbf{v} - (\mathbf{v} \cdot \mathbf{r}_i) \mathbf{r}_i$$

and

$$(\mathbf{g}_i \mathbf{h}_1)_T(\mathbf{r}_i) := \mathbf{g}_i \mathbf{h}_1 - (\mathbf{g}_i \mathbf{h}_1 \cdot \mathbf{r}_i) \mathbf{r}_i,$$

for which

$$\begin{aligned}
 (\mathbf{g}_i \mathbf{h}_1)_T(\mathbf{r}_i) &= \mathbf{g}_i \mathbf{h}_1 - (\mathbf{g}_i \mathbf{h}_1 \cdot \mathbf{g}_i \mathbf{h}) \mathbf{g}_i \mathbf{h} \\
 &= \mathbf{g}_i \mathbf{h}_1 - (\mathbf{h}_1 \cdot \mathbf{h}) \mathbf{g}_i \mathbf{h} \\
 &= \mathbf{g}_i [\mathbf{h}_1 - (\mathbf{h}_1 \cdot \mathbf{h}) \mathbf{h}]
 \end{aligned}$$

holds.

Then

$$\begin{aligned}
 \cos \omega(\mathbf{r}_i) &= \frac{(\mathbf{v})_T(\mathbf{r}_i) \cdot (\mathbf{g}_i \mathbf{h}_1)_T(\mathbf{r}_i)}{\|(\mathbf{v})_T(\mathbf{r}_i)\| \|(\mathbf{g}_i \mathbf{h}_1)_T(\mathbf{r}_i)\|} \\
 &= \frac{(\mathbf{v})_T(\mathbf{r}_i) \cdot (\mathbf{g}_i \mathbf{h}_1)_T(\mathbf{r}_i)}{[1 - (\mathbf{v} \cdot \mathbf{r}_i)^2]^{1/2} [1 - (\mathbf{h}_1 \cdot \mathbf{h})^2]^{1/2}}, \quad (11)
 \end{aligned}$$

where $\omega(\mathbf{r}_i) \in [0, \pi)$ if $(\mathbf{v})_T(\mathbf{r}_i) \times (\mathbf{g}_i \mathbf{h}_1)_T(\mathbf{r}_i)$ is parallel to \mathbf{r}_i , and $\omega \in [\pi, 2\pi)$ if $(\mathbf{v})_T(\mathbf{r}_i) \times (\mathbf{g}_i \mathbf{h}_1)_T(\mathbf{r}_i)$ is antiparallel to \mathbf{r}_i (see Figs. 1 and 2a). Computationally, we use the form

$$\omega(\mathbf{r}_i) = \text{atan2}\{(\mathbf{v})_T(\mathbf{r}_i) \cdot [(\mathbf{g}_i \mathbf{h}_1)_T(\mathbf{r}_i) \times \mathbf{r}_i], (\mathbf{v})_T(\mathbf{r}_i) \cdot (\mathbf{g}_i \mathbf{h}_1)_T(\mathbf{r}_i)\},$$

where $\text{atan2}(x, y)$ is a function of two arguments giving the angle of the complex number $x + iy$, available in most computer languages.

Subsequently, we shall omit the argument \mathbf{r}_i of ω . We have chosen to denote our type of sections as ω sections, as ω actually refers to an orientation distance. In greater detail, for each location \mathbf{r} of any \mathbf{h} -pole figure, ω is the specific orientation distance between the actual orientation mapping \mathbf{h} onto \mathbf{r} and a reference orientation mapping both \mathbf{h} onto \mathbf{r} and simultaneously \mathbf{h}_1 onto \mathbf{v} . Since an orientation distance is always also a rotation angle of some rotation, we have specified this rotation as a rotation about \mathbf{r} through the angle ω .

Thus, the \mathbf{h} -pole point plot

$$P_n(\mathbf{g}; \mathbf{h}, \mathbf{r}) = \sum_{i=1}^n \mathbf{I}_{\{\mathbf{g}, \mathbf{h}=\mathbf{r}\}}(\mathbf{g}) \quad (12)$$

can be spread into ω sections defined as

$$P_n(\mathbf{g}; \mathbf{h}, \mathbf{r}; \mathbf{h}_1, \mathbf{v}, \omega) = \sum_{i=1}^n \mathbf{I}_{\{\mathbf{g}, \mathbf{h}=\mathbf{r} \text{ and } \angle[(\mathbf{v})_T(\mathbf{r}), (\mathbf{g}_i \mathbf{h}_1)_T(\mathbf{r})] = \omega\}}(\mathbf{g}), \quad (13)$$

the superposition of which with respect to ω is the \mathbf{h} -pole point plot.

For the purpose of visualization, a tolerance measure $\Delta\omega$ has to be applied, and the ω sections actually displayed are defined as indicators of $G(\mathbf{h}, \mathbf{r}, \mathbf{h}_1, \mathbf{v}, \omega, \Delta\omega) \subset G(\mathbf{h}, \mathbf{r})$ by

$$P_n(\mathbf{g}; \mathbf{h}, \mathbf{r}; \mathbf{h}_1, \mathbf{v}, \omega, \Delta\omega) = \sum_{i=1}^n \mathbf{I}_{G(\mathbf{h}, \mathbf{r}, \mathbf{h}_1, \mathbf{v}, \omega, \Delta\omega)}(\mathbf{g}),$$

with

$$\begin{aligned}
 G(\mathbf{h}, \mathbf{r}, \mathbf{h}_1, \mathbf{v}, \omega, \Delta\omega) &:= \{\mathbf{g} \in SO(3) \mid \mathbf{g}\mathbf{h} = \mathbf{r} \text{ and} \\
 &\quad \angle[(\mathbf{v})_T(\mathbf{r}), (\mathbf{g}_i \mathbf{h}_1)_T(\mathbf{r})] \in [\omega - \Delta\omega, \omega + \Delta\omega]\} \quad (14)
 \end{aligned}$$

It should be noted that the set $G(\mathbf{h}, \mathbf{r}, \mathbf{h}_1, \mathbf{v}, \omega, 0)$ determines a unique orientation.

Thus, the orientations \mathbf{g}_i displayed as points $\mathbf{r}_i = \mathbf{g}_i \mathbf{h}$ augmented with $\mathbf{g}_i \mathbf{h}_1$ orthogonally projected onto the tangential plane at \mathbf{r}_i are sorted according to ω as defined in equation (11). Using the same projection onto the unit disk as for the \mathbf{h} -pole points results in plots of ω sections of the

orientation space with the same properties as the \mathbf{h} -pole point plot.

4. Integral measurements of diffraction pole probability density functions

4.1. Special case

Obviously,

$$\mathbf{g}(\alpha, \beta, \gamma) \begin{pmatrix} 0 \\ 0 \\ 1 \end{pmatrix}_{K_C} = \begin{pmatrix} \cos \alpha \sin \beta \\ \sin \alpha \sin \beta \\ \cos \beta \end{pmatrix}_{K_S} =: \mathbf{r}_{K_S} \text{ for all } \gamma \in [0, 2\pi),$$

and

$$\mathbf{g}^{-1}(\alpha, \beta, \gamma) \begin{pmatrix} 0 \\ 0 \\ 1 \end{pmatrix}_{K_S} = \begin{bmatrix} \cos(\pi - \gamma) \sin \beta \\ \sin(\pi - \gamma) \sin \beta \\ \cos \beta \end{bmatrix}_{K_C} =: \mathbf{h}'_{K_C}$$

for all $\alpha \in [0, 2\pi)$.

Let $f : SO(3) \mapsto \mathbb{R}^1$ denote an orientation probability density function $f \in \mathcal{L}^1[SO(3)]$. Then,

$$\begin{aligned}
 \frac{1}{2\pi} \int_{[0, 2\pi]} f[g(\alpha, \beta, \gamma)] d\gamma &= \frac{1}{2\pi} \int_{\{\mathbf{g} \in SO(3) \mid \mathbf{g}\mathbf{e}_3 = \mathbf{r}\}} f(\mathbf{g}) d\mathbf{g} \\
 &= (\mathcal{R}_1 f)(\mathbf{z}_{K_C}, \mathbf{r}_{K_S}), \quad (15)
 \end{aligned}$$

which is the spherical probability density function of the crystallographic direction \mathbf{z}_{K_C} , and

$$\begin{aligned}
 \frac{1}{2\pi} \int_{[0, 2\pi]} f[g(\alpha, \beta, \gamma)] d\alpha &= \frac{1}{2\pi} \int_{\{\mathbf{g} \in SO(3) \mid \mathbf{g}\mathbf{h}' = \mathbf{e}_3\}} f(\mathbf{g}) d\mathbf{g} \\
 &= (\mathcal{R}_1 f)(\mathbf{h}'_{K_C}, \mathbf{z}_{K_S}), \quad (16)
 \end{aligned}$$

or

$$\frac{1}{2\pi} \int_{[0, 2\pi]} f[g(\alpha, \beta, \pi - \gamma)] d\alpha = (\mathcal{R}_1 f)(\mathbf{h}_{K_C}, \mathbf{z}_{K_S}),$$

respectively, which is the spherical probability density function of the specimen direction \mathbf{z}_{K_S} . Analogous relations hold for differently defined Euler angles.

In these instances, averaging may be thought of as providing a projection of $f : S^2 \times [0, 2\pi] \mapsto \mathbb{R}^1_+$ onto S^2 , and eventually onto the unit disk $D \subset \mathbb{R}^2$ when some projection $S^2 \mapsto D$ is applied. If $f(\alpha, \beta, \gamma)$ is displayed in plane γ sections (of fixed γ), then their superposition is the spherical probability density function of the crystallographic \mathbf{z}_{K_C} direction. If the same projection onto the unit disk is used for γ sections and for the spherical probability density function $(\mathcal{R}_1 f)(\mathbf{z}_{K_C}, \mathbf{r}_{K_S})$, then they have the same properties in common.

Analogously, if f is displayed in α sections of fixed α , then their superposition is the spherical probability density function of the specimen \mathbf{z}_{K_S} direction.

Let $\gamma_i := 2\pi i/p$, $i = 0, \dots, p$, denote a partition of $[0, 2\pi]$ into equidistant intervals $[\gamma_{i-1}, \gamma_i]$ with $\Delta\gamma = \gamma_i - \gamma_{i-1}$, $i = 1, \dots, p$, and $0 = \gamma_0 = \gamma_p \bmod 2\pi$. Instead of displaying $f(\alpha, \beta, \gamma_i)$,

$i = 1, \dots, n$, a smoothed γ section can be defined in this instance as

$$(\Gamma_{if})(\mathbf{z}_{K_c}, \mathbf{r}_{K_s}) = \frac{1}{2\pi} \int_{[\gamma_i - \frac{1}{2}\Delta\gamma, \gamma_i + \frac{1}{2}\Delta\gamma]} f[g(\alpha, \beta, \gamma)] d\gamma \quad (17)$$

with

$$(\mathcal{R}_1 f)(\mathbf{z}_{K_c}, \mathbf{r}_{K_s}) = \sum_{i=1}^p (\Gamma_{if})(\mathbf{z}_{K_c}, \mathbf{r}_{K_s}). \quad (18)$$

Since the elements of $G(\mathbf{z}_{K_c}, \mathbf{r}_i)$ differ by an initial rotation about \mathbf{z}_{K_c} , or a final rotation about \mathbf{r}_i , respectively, by an angle $\gamma \in [0, 2\pi)$, the physical significance of γ is that it is very closely related to the angle ω between the orthogonal projection of $\mathbf{g} \mathbf{x}_{K_c}$ and the orthogonal projection of the specimen direction \mathbf{z}_{K_s} onto the tangential plane at $\mathbf{r}_{K_s} = \mathbf{g} \mathbf{z}_{K_c}$. On several occasions when γ sections were introduced, this relationship was neither explicitly recognized nor particularly

appreciated (*cf.* Kocks *et al.*, 1999). In fact, by the very definition of Euler angles, it holds for $\gamma = 0$ that

$$\mathbf{g}(\alpha, \beta, \gamma) \mathbf{x}_{K_c} = \begin{pmatrix} \cos \alpha \cos \beta \\ \sin \alpha \cos \beta \\ -\sin \beta \end{pmatrix} = \begin{bmatrix} \cos \alpha \sin(\pi/2 + \beta) \\ \sin \alpha \sin(\pi/2 + \beta) \\ \cos(\pi/2 + \beta) \end{bmatrix}.$$

Thus, the three directions $\mathbf{g} \mathbf{x}_{K_c}$, \mathbf{z}_{K_s} and $\mathbf{g} \mathbf{z}_{K_c}$ belong to one plane orthogonal to the tangential plane at $\mathbf{r}_{K_s} = \mathbf{g} \mathbf{z}_{K_c}$. The sign of the z components of the former two directions indicates that the angle ω between their orthogonal projections is π . Corresponding to $\gamma = \pi$, the angle ω between the projections of $\mathbf{g}(-\mathbf{x}_{K_c})$ and \mathbf{z}_{K_s} onto the plane vanishes.

For arbitrary γ , this can be seen by elementary arguments as follows. With $\mathbf{v} = \mathbf{z}_{K_s}$ and $\mathbf{h}_1 = \mathbf{x}_{K_c}$,

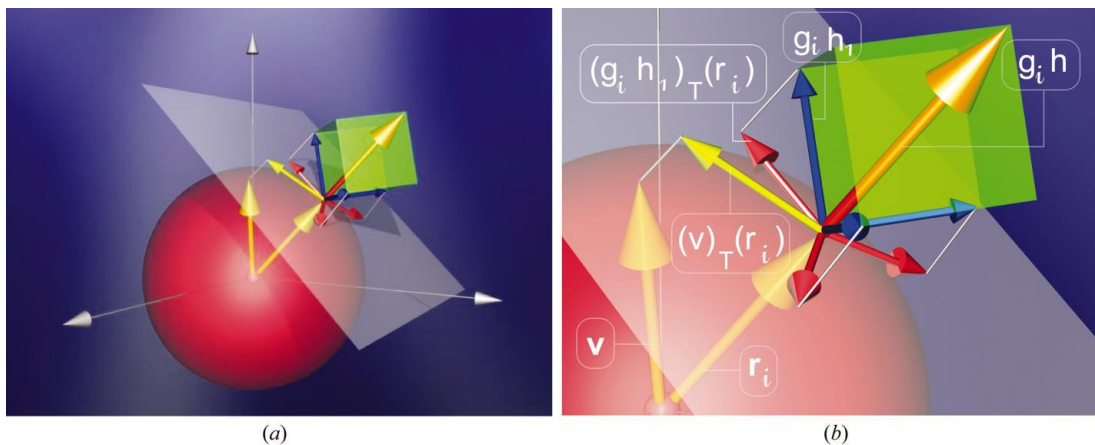


Figure 1 (111)-pole sphere displaying $(111)^f = \mathbf{h} = \mathbf{g}_i^{-1} \mathbf{r}_i$, and the associated tangential plane with the orthogonal projection of the crystal direction $\mathbf{h}_1 = (100)^f$, represented by $\mathbf{g}_i \mathbf{h}_1$ with respect to the specimen coordinate system K_s , and its crystal-symmetry equivalents, and the orthogonal projection of the specimen direction \mathbf{v} , enclosing the angle ω . (Figures courtesy of Heiko Kost, Anidesk Digitalvisualization, Webenheim, Germany.)

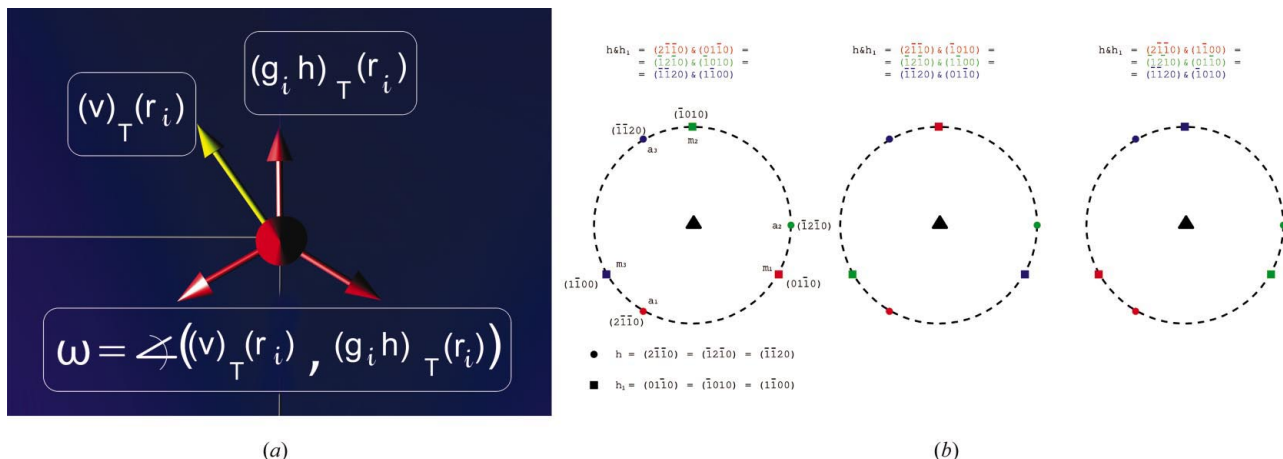


Figure 2 Top view of the tangential plane with the orthogonal projection of the crystal direction $\mathbf{h}_1 = (100)^f$, represented by $\mathbf{g}_i \mathbf{h}_1$ with respect to the specimen coordinate system K_s , and its crystal-symmetry equivalents, and the orthogonal projection of the specimen direction \mathbf{v} , enclosing the angle ω . [Part (a) courtesy of Heiko Kost, KPMG InfoDesign, Saarbrücken, Germany.]

$$\begin{aligned} \mathbf{v}_1 &= \frac{\mathbf{z}_{K_S} - (\mathbf{z}_{K_S} \cdot \mathbf{r}) \mathbf{r}}{\|\mathbf{z}_{K_S} - (\mathbf{z}_{K_S} \cdot \mathbf{r}) \mathbf{r}\|} \\ &= \frac{1}{\sin \beta} \left[\begin{pmatrix} 0 \\ 0 \\ 1 \end{pmatrix} - \cos \beta \begin{pmatrix} \cos \alpha \sin \beta \\ \sin \alpha \sin \beta \\ \cos \beta \end{pmatrix} \right] \\ &= \begin{pmatrix} -\cos \alpha \cos \beta \\ -\sin \alpha \cos \beta \\ \sin \beta \end{pmatrix} \end{aligned}$$

and

$$\begin{aligned} \mathbf{v}_2 &= \mathbf{g} \mathbf{x}_{K_C} - (\mathbf{x}_{K_C} \cdot \mathbf{z}_{K_C}) \mathbf{r} \\ &= \mathbf{g} \mathbf{x}_{K_C} \\ &= \begin{pmatrix} \cos \alpha \cos \beta \cos \gamma - \sin \alpha \sin \gamma \\ \sin \alpha \cos \beta \cos \gamma + \cos \alpha \sin \gamma \\ -\sin \beta \cos \gamma \end{pmatrix}. \end{aligned}$$

Thus,

$$\mathbf{v}_1 \cdot \mathbf{v}_2 = \cos(\pi - \gamma),$$

from which the angle ω between the orthogonal projection of $\mathbf{g} \mathbf{x}_{K_C}$, i.e. \mathbf{v}_2 , being anticlockwise rotated by γ about \mathbf{r} , and \mathbf{v}_1 , which is the orthogonally projected \mathbf{z}_{K_S} , is interpreted as

$$\omega = \angle(\mathbf{v}_2, \mathbf{v}_1) = \pi - \gamma$$

when \mathbf{v}_2 , \mathbf{v}_1 and \mathbf{r} are thought of as a right-handed system.

4.2. General case

In mathematical tomography, the transform that assigns to a function, defined on a d -dimensional manifold, its mean values with respect to the family of d' -dimensional submanifolds, with $1 \leq d' \leq d - 1$, is referred to as a d' -plane transform or Radon $\mathcal{R}_{d'}$ transform. If $d' = 1$, \mathcal{R}_1 is sometimes explicitly called the X-ray transform; if $d' = d - 1$, it is referred to as the Radon transform \mathcal{R} . For $d = 2$, the two cases coincide. However, the term ‘spherical X-ray transform’ is not used here to avoid confusion with the spherical crystallographic X-ray transform to be properly defined below. It is emphasized that in either case the term ‘X-ray transform’ does not refer to the actual radiation, which could be X-ray, γ , neutron or synchrotron radiation. In the mathematical sense, the term ‘spherical crystallographic X-ray transform’ will generally apply to texture analysis and is used by us (cf. Cerejeiras *et al.*, 2002). The origins of spherical mathematical tomography date back to the pioneering papers by Funk (1913, 1916), while mathematical tomography in a Euclidean setting appeared later with the classic paper by Radon (1917).

Generally, the spherical Radon transform \mathcal{R}_1 associating a function $\mathcal{R}_1 f : (S^2 \times S^2) \mapsto \mathbb{R}^1_+$ with an orientation probability density function $f : SO(3) \mapsto \mathbb{R}^1_+$ is defined as (Helgason, 1959; Bunge, 1969; Schaeben *et al.*, 2001)

$$(\mathcal{R}_1 f)(\mathbf{h}, \mathbf{r}) := \frac{1}{2\pi} \int_{\{\mathbf{g} \in SO(3) | \mathbf{g} \mathbf{h} = \mathbf{r}\}} f(\mathbf{g}) \, d\mathbf{g} = \frac{1}{2\pi} \int_{G(\mathbf{h}, \mathbf{r})} f(\mathbf{g}) \, d\mathbf{g}. \quad (19)$$

The general axes probability density function associated with an orientation probability density function f is defined as

$$(\mathcal{A}f)(\mathbf{h}, \mathbf{r}) = \frac{1}{2} [(\mathcal{R}f)(\mathbf{h}, \mathbf{r}) + (\mathcal{R}f)(-\mathbf{h}, \mathbf{r})].$$

$(\mathcal{A}f)$ is also referred to as the bi-axial probability density function.

The basic crystallographic X-ray transform, i.e. the pole probability density function, associated with the crystal form H of an orientation probability density function f , is provided by mean values of $\mathcal{R}_1 f$,

$$(\mathcal{X}f)(\mathbf{h}, \mathbf{r}) = \frac{1}{2 \text{card}(H)} \sum_{\mathbf{h} \in H} [(\mathcal{R}_1 f)(\mathbf{h}, \mathbf{r}) + (\mathcal{R}_1 f)(-\mathbf{h}, \mathbf{r})].$$

Considering \mathbf{h} as a parameter rather than as a variable, $(\mathcal{X}f)$ is usually called the ‘ \mathbf{h} -pole probability density function’; considering \mathbf{r} as a parameter, it is usually called the ‘inverse \mathbf{r} -pole probability density function’.

Analogously to the special case of $(\mathcal{R}_1 f)(\mathbf{z}_{K_C}, \mathbf{r}_{K_S})$, or $(\mathcal{X}f)(\mathbf{z}_{K_C}, \mathbf{r}_{K_S})$, respectively, any \mathbf{h} -pole probability density plot can be spread into ω sections, now defined with appropriate additional directions \mathbf{h}_1 and \mathbf{v} as

$$\begin{aligned} (\Omega f)(\mathbf{h}, \mathbf{r}; \mathbf{h}_1, \mathbf{v}, \omega, \Delta\omega) \\ = \frac{1}{2} \left\{ \frac{1}{2\pi} \left[\int_{G(\mathbf{h}, \mathbf{r}; \mathbf{h}_1, \mathbf{v}, \omega, \Delta\omega)} + \int_{G(-\mathbf{h}, \mathbf{r}; \mathbf{h}_1, \mathbf{v}, \omega, \Delta\omega)} \right] f(\mathbf{g}) \, d\mathbf{g} \right\}, \end{aligned} \quad (20)$$

with $G(\mathbf{h}, \mathbf{r}; \mathbf{h}_1, \mathbf{v}, \omega, \Delta\omega)$ as defined in equation (14).

Referring to the quaternionic notation (cf. Schaeben *et al.*, 2001; Cerejeiras *et al.*, 2002), the Radon \mathcal{R}_1 transform may be rewritten as

$$(\mathcal{R}_1 f)(\mathbf{h}, \mathbf{r}) = \frac{1}{2\pi} \int_{[0, 2\pi]} f[q(t)] \, dt, \quad (21)$$

where $q(t)$ varies along the circle of all quaternions with $\mathbf{h} = q^* \mathbf{r} q$ as t varies in $[0, 2\pi]$. This circle is properly defined by

$$C(q_1, q_2) = \{q(t) \in S^3 \mid q(t) = q_1 \cos t + q_2 \sin t, \quad t \in [0, 2\pi]\} \quad (22)$$

with

$$q_1 = \frac{1}{\|1 - r\mathbf{h}\|} (1 - r\mathbf{h}) = \cos \frac{\eta}{2} + \frac{\mathbf{h} \times \mathbf{r}}{\|\mathbf{h} \times \mathbf{r}\|} \sin \frac{\eta}{2}$$

and

$$q_2 = \frac{1}{\|h + r\|} (h + r) = 0 + \frac{\mathbf{h} + \mathbf{r}}{\|\mathbf{h} + \mathbf{r}\|},$$

where

$$\|1 - r\mathbf{h}\| = [2(1 + \cos \eta)]^{1/2}$$

and

$$\|h + r\| = 2 \cos \frac{\eta}{2},$$

in which $\cos \eta = \mathbf{h} \cdot \mathbf{r}$. Obviously, $\|1 - r\mathbf{h}\| = \|h + r\|$. Thus, in greater detail,

$$\text{Sc } q(t) = \cos \frac{\omega(t)}{2} = \cos \frac{\eta}{2} \cos t \quad (23)$$

and

$$\begin{aligned} \text{Vec } q(t) &= \sin \frac{\omega(t)}{2} \frac{\mathbf{q}(t)}{\|\mathbf{q}(t)\|} \\ &= \sin \frac{\omega(t)}{2} \left[\frac{\mathbf{h} \times \mathbf{r}}{\sin \eta} \cos t + \frac{\mathbf{h} + \mathbf{r}}{2 \cos(\eta/2)} \sin t \right] \\ &= \frac{1}{2 \cos(\eta/2)} [(\mathbf{h} \times \mathbf{r}) \cos t + (\mathbf{h} + \mathbf{r}) \sin t]. \end{aligned} \quad (24)$$

Thus, the angles of rotations of the circle (22) vary according to equation (23), and the axes of rotations vary in the plane spanned by the axes of the rotations represented by q_1 and q_2 , *i.e.* by

$$\mathbf{n}_1 = \frac{\mathbf{h} \times \mathbf{r}}{\sin \eta} \quad \text{and} \quad \mathbf{n}_2 = \frac{\mathbf{h} + \mathbf{r}}{2 \cos(\eta/2)},$$

while t varies in $[0, 2\pi]$. The plane of the axes of rotations of the circle [equation (22)] is uniquely given by its unit normal

$$\mathbf{n}_1 \times \mathbf{n}_2 = \left(\frac{\mathbf{h} \times \mathbf{r}}{\sin \eta} \right) \times \left[\frac{\mathbf{h} + \mathbf{r}}{2 \cos(\eta/2)} \right] = \frac{\mathbf{r} - \mathbf{h}}{2 \sin(\eta/2)}.$$

It should be noted that

$$r q_1 = q_1 h = q_2.$$

Defining now the quaternions

$$h(t) = \cos t + \mathbf{h} \sin t, \quad t \in [0, 2\pi)$$

and

$$r(t) = \cos t + \mathbf{r} \sin t, \quad t \in [0, 2\pi),$$

representing rotations about \mathbf{h} or \mathbf{r} , respectively, by an arbitrary angle $t \in [0, 2\pi)$, it holds that

$$C(q_1, q_2) = \{q_0 h(t) \mid t \in [0, 2\pi)\} \quad (25)$$

and also

$$C(q_1, q_2) = r(t) q_0 \mid t \in [0, 2\pi)$$

for any $q_0 \in S^3$ with

$$q_0 \mathbf{h} q_0^* = \mathbf{r}, \quad (26)$$

i.e. for any $q_0 \in C(q_1, q_2)$. In particular, with the choice $q_0 = q_1$ it holds that

$$q(t) = r(t) q_1, \quad t \in [0, 2\pi),$$

as, obviously, $q_0 = q_1$, and $q(\pi/2) = q_1 h(\pi/2) = q_1 h = q_2$. Of course, the decomposition [equation (25)] of elements of $C(q_1, q_2)$ corresponds to the decomposition [equation (8)] of matrices. Since condition (26) does not uniquely determine q_0 , there is a freedom of choice which could be utilized to choose q_0 such that

$$q_0 \mathbf{h} q_0^* = \mathbf{r} \quad \text{and} \quad q_0 \mathbf{h}_1 q_0^* = \mathbf{v}, \quad (27)$$

where the second part would ensure that

$$\angle[(\mathbf{v})_T(\mathbf{r}), (\mathbf{g}_0 \mathbf{h}_1)_T(\mathbf{r})] = 0.$$

Algebraically, q_0 is given as the solution of the system of the two equations

$$q_0 \mathbf{h} - \mathbf{r} q_0 = 0 \quad (28)$$

and

$$q_0 \mathbf{h}_1 - \mathbf{v} q_0 = 0, \quad (29)$$

subject to

$$\mathbf{h} \cdot \mathbf{h}_1 = \mathbf{r} \cdot \mathbf{v}. \quad (30)$$

By geometrical reasoning (Meister, 1997; Meister & Schaeben, 2004), the solution is given as follows. The axis \mathbf{n}_0 of the rotation q_0 is given by the intersection of the two planes of rotation axes corresponding to circle (28) and circle (29), respectively. The intersection of two planes is provided by the vector product of their normals:

$$\begin{aligned} \mathbf{n}_0 &= \left[\left(\frac{\mathbf{h} \times \mathbf{r}}{\|\mathbf{h} \times \mathbf{r}\|} \right) \times \left(\frac{\mathbf{h} + \mathbf{r}}{\|\mathbf{h} + \mathbf{r}\|} \right) \right] \\ &\quad \times \left[\left(\frac{\mathbf{h}_1 \times \mathbf{v}}{\|\mathbf{h}_1 \times \mathbf{v}\|} \right) \times \left(\frac{\mathbf{h}_1 + \mathbf{v}}{\|\mathbf{h}_1 + \mathbf{v}\|} \right) \right]. \end{aligned}$$

The angle ω_0 of the rotation q_0 is provided by

$$\tan \frac{\omega_0}{2} = \frac{\sin \eta}{\sin \zeta (\cos \eta + 1)},$$

or equivalently by

$$\cos \omega_0 = \frac{(\mathbf{n}_0 \times \mathbf{r})^t (\mathbf{n}_0 \times \mathbf{h})}{\|\mathbf{n}_0 \times \mathbf{r}\| \|\mathbf{n}_0 \times \mathbf{h}\|},$$

where ζ denotes the angle between the axis \mathbf{n}_0 and the plane spanned by \mathbf{h} and \mathbf{r} (*cf.* Meister, 1997, pp. 59–60).

However, for varying \mathbf{r} and fixed \mathbf{h} , \mathbf{h}_1 and \mathbf{v} , the constraint (30) is much too restrictive because it can usually not be satisfied. Therefore, the criterion (27) to choose q_0 is relaxed to

$$q_0 \mathbf{h} q_0^* = \mathbf{r} \quad \text{and} \quad (q_0 \mathbf{h}_1 q_0^*)_T(\mathbf{r}) = (\mathbf{v})_T(\mathbf{r}). \quad (31)$$

For an arbitrary but fixed $q \in C(q_1, q_2)$, it holds that

$$r(t) q \mathbf{h} q^* r^*(t) = \mathbf{r}$$

and

$$\begin{aligned} [r(t) q \mathbf{h}_1 q^* r^*(t)]_T(\mathbf{r}) &= r(t) q \mathbf{h}_1 q^* r^*(t) - (\mathbf{h}_1 \cdot \mathbf{h}) \mathbf{r} \\ &= r(t) q \mathbf{h}_1 q^* r^*(t) - r(t) (\mathbf{h}_1 \cdot \mathbf{h}) \mathbf{r} r^*(t) \\ &= r(t) (q \mathbf{h}_1 q^*)_T(\mathbf{r}) r^*(t) \end{aligned}$$

for all $t \in [0, 2\pi)$. Choosing

$$t_0 := \arccos[(q \mathbf{h}_1 q^*)_T(\mathbf{r}) \cdot (\mathbf{v})_T(\mathbf{r})],$$

the second part of equation (31) is satisfied for $q_0 := r(t_0)q$.

To retrieve the Euler angles $(\alpha_0, \beta_0, \gamma_0)$ parametrizing the rotation represented by q_0 requires the evaluation of $r(t_0)q$ and the application of the formula given, for example, by Altmann (1986).

Eventually, the corresponding ω section may be rewritten as

$$(\Omega f)(\mathbf{h}, \mathbf{r}; \mathbf{h}_1, \mathbf{v}, \omega, \Delta\omega) = \frac{1}{2} \int_{[\omega-\Delta\omega, \omega+\Delta\omega]} f[r(t)q_0] dt \quad (32)$$

if now the orthogonal projections $(\mathbf{g}\mathbf{h}_1)_T(\mathbf{r})$, $(\mathbf{v})_T(\mathbf{r})$ and \mathbf{r} are thought of as a right-handed coordinate system.

In particular, the set of orientations $G(\mathbf{h}, \mathbf{r}; \mathbf{h}_1, \mathbf{v}, \omega, 0)$ contains a single orientation $\mathbf{g} \in G$, and ω sections are reduced to displays of the orientation probability density function $f(\mathbf{g})$ at the corresponding point of the \mathbf{h} -pole point plot using contour-level lines and/or shaded iso-planes.

When highlighting is to be applied to display an orientation probability density function, a display of the \mathbf{h} -pole density of a selected set of orientations in a view already displaying the \mathbf{h} -pole density of all orientations is required. A set of orientations (which is now an infinite set) is selected in one view of orientations with specific pole directions; the other views will display which specimen directions are preferred by other crystallographic directions for that set. The conditional density \mathbf{h} given that \mathbf{g} is in the selected set provides the required information. The idea is to use contouring and to display iso-planes of the two densities with two totally different colour scales. The unselected density is displayed with a grey scale. The conditional density of the selected set is displayed in a coloured scale. Thus the two sets can easily be distinguished. At every point of the pole density plot, the larger density is displayed. Optionally, one of the displays may be switched off or the contour lines may be added on top of the other iso-planes, which allows a numerical comparison of two pole densities.

5. General definition of ω sections of the orientation space

An ω section of the orientation space is defined in terms of the following three parameters.

(i) A parameter \mathbf{g}_0 defining the orientation of the specimen coordinate system K_S with respect to some external coordinate system K .

(ii) A crystallographic direction \mathbf{h} characterizing the pole point or pole probability density plot, which is the superposition of all sections. An orientation g is initially incompletely displayed at location $\mathbf{r} = \mathbf{g}\mathbf{h}$ and at all locations corresponding to crystal-symmetry-equivalent directions of \mathbf{h} .

(iii) A second crystallographic direction \mathbf{h}_1 , not parallel to \mathbf{h} , a specimen direction \mathbf{v} , not parallel to \mathbf{r} , an angle $\omega \in [0, 2\pi]$, and an angular tolerance $\Delta\omega$. An orientation is actually displayed if and only if the angle of \mathbf{h}_1 and \mathbf{v} , both orthogonally projected onto the tangential plane of the \mathbf{h} -pole sphere at \mathbf{r}_0 , is in $[\omega - \Delta\omega, \omega + \Delta\omega]$, *i.e.*

$$\angle[(\mathbf{v})_T(\mathbf{r}), (\mathbf{g}\mathbf{h}_1)_T(\mathbf{r})] \in [\omega + \Delta\omega, \omega - \Delta\omega].$$

Operationally, an ω section of the orientation space is defined for integral measurements by

$$\begin{aligned} (\Omega f)(\mathbf{h}, \mathbf{r}; \mathbf{h}_1, \mathbf{v}, \omega, \Delta\omega) &= \frac{1}{2} \int_{[\omega-\Delta\omega, \omega+\Delta\omega]} f[r(t)q_0] dt \\ &= \frac{1}{2} \int_{[\omega-\Delta\omega, \omega+\Delta\omega]} f[\mathbf{g}(\varpi; \mathbf{r})\mathbf{g}_0] d\varpi, \end{aligned}$$

and for individual measurements by

$$P_n(\mathbf{g}; \mathbf{h}, \mathbf{r}; \mathbf{h}_1, \mathbf{v}, \omega, \Delta\omega) = \sum_{i=1}^n \mathbf{I}_{\{\mathbf{g}_0, \mathbf{g}(\omega; \mathbf{h}) \mid \omega \in [\omega-\Delta\omega, \omega+\Delta\omega]\}}(\mathbf{g}),$$

with the unit quaternion $q_0 \in \mathcal{S}^3$ representing the rotation \mathbf{g}_0 such that $q_0 \mathbf{h} q_0^* = \mathbf{r}$ and $(q_0 \mathbf{h}_1 q_0^*)_T(\mathbf{r}) = q_0(\mathbf{h}_1)_T(\mathbf{r})q_0^* = (\mathbf{v})_T(\mathbf{r})$, where \mathbf{h}, \mathbf{r} is a pair comprising a crystallographic direction and a specimen direction, \mathbf{h}_1 is an additional crystallographic direction, and \mathbf{v} is an additional specimen direction, which are all presumed to be given, *i.e.* they have to be specified by the user, as have ω and $\Delta\omega$.

5.1. ω sections and crystal symmetry

Considering crystal symmetry is straightforward. Every crystal is displayed in each of its crystallographic equivalent orientations throughout the sections, *i.e.* a specified crystal direction \mathbf{h} , and all its symmetry equivalents $\mathbf{g}\mathbf{c}\mathbf{h}$ are plotted at the locations $\mathbf{r}_i^c = \mathbf{g}_i\mathbf{c}\mathbf{h}$ provided by the orientation \mathbf{g}_i .

It should be noted that the joint symmetry of the pair $(\mathbf{h}, \mathbf{h}_1)$ is in general different from the symmetry of \mathbf{h} and \mathbf{h}_1 individually. Thus it matters which representatives of the sets of equivalents of \mathbf{h} and \mathbf{h}_1 we choose because different representatives can lead to different equivalence classes of pairs $(\mathbf{h}, \mathbf{h}_1)$ and eventually to apparently different ω sections. As an example, we consider the simple case of trigonal symmetry 3, $\mathbf{h} = \mathbf{a} = (2\bar{1}\bar{1}0)$ and $\mathbf{h}_1 = \mathbf{m} = (01\bar{1}0)$. These two planes enclose an angle of $\pi/2$, which is preserved by crystal symmetry, leading to three equivalent pairs $[(2\bar{1}\bar{1}0), (01\bar{1}0)]$, $[(\bar{1}2\bar{1}0), (\bar{1}010)]$ and $[(\bar{1}\bar{1}20), (1\bar{1}00)]$. However, choosing instead $(\bar{1}010)$ as representative of the crystal plane \mathbf{h}_1 leads to a constant angle of $5\pi/6$ and to three different pairs, $[(2\bar{1}\bar{1}0), (\bar{1}010)]$, $[(\bar{1}2\bar{1}0), (1\bar{1}00)]$ and $[(\bar{1}\bar{1}20), (01\bar{1}0)]$. The orthogonal projections of \mathbf{h}_1 of these pairs onto the tangential plane at $\mathbf{g}\mathbf{h}$ differ by an angle of π from the projections of \mathbf{h}_1 of the first three pairs. Thus, the ω sections differ by a rotation through π for this example.

The three essentially different sets of pairs given by $\mathbf{h} = \mathbf{a}_{1,2,3}$ and $\mathbf{h}_1 = \mathbf{m}_{1,2,3}$ are displayed in Fig 2(b).

In summary, without any additional provision, ω sections distinguish the direction \mathbf{h}_1 , which makes an angle of $\pi/2$ with \mathbf{h} , from its equivalents, which make angles of $5\pi/6$ and $3\pi/2$, respectively. Although these directions are physically equivalent they can be distinguished by their angle with the sample direction \mathbf{r} of \mathbf{h} , which is given by the location in the pole figure.

As an interesting consequence, whenever \mathbf{h} is an n -fold (rotation or rotation-inversion) axis, we have n equivalent pairs $(\mathbf{h}, \mathbf{h}_1)$ with the same representative of \mathbf{h} and thus with the same sample direction \mathbf{r} . Therefore the ω sections for

$\omega \in [0, 2\pi/n)$ are repeated n times for $\omega \in [0, 2\pi)$, and it is thus sufficient to plot the ω sections for $\omega \in [0, 2\pi/n)$ only.

6. Properties of ω sections

The essential properties of ω sections may be listed as follows.

(a) ω sections preserve volume, respectively area, if equal-area projection of the pole sphere on the unit disk is applied.

(b) The direction of any given axis with respect to the reference frame is geometrically visible.

(c) The defining parameters have a simple geometrical interpretation.

(d) The user can choose the most informative sections in a fast and interactive way.

(e) ω sections add up to a user-specified pole probability density function.

(f) The set of sections visualizes the complete information of the orientation probability density function.

Dynamically linked views of ω sections and their superposition will provide easy-to-read and instructive displays of the orientation data, their probability density function and corresponding pole probability density functions. In this way, ω sections can be instrumental for exploratory data analysis like ‘how does a given crystal direction \mathbf{h}_1 relate with a given specimen direction \mathbf{v} , e.g. second principal stress direction?’.

If $\omega = 0$, then all orientations are actually displayed for which \mathbf{h}_1 is perfectly aligned with \mathbf{v} and \mathbf{h} coincides with the direction \mathbf{r} displayed in the \mathbf{h} -pole point plot. If $\omega = \pi/2$ or $\omega = \pi$, then all orientations are displayed for which \mathbf{h}_1 is largely misaligned with \mathbf{v} and \mathbf{h} coincides with the direction \mathbf{r} displayed in the \mathbf{h} -pole point plot.

Visualizing the angle ω in a circular display and continuously varying ω along the circle $[0, 2\pi]$, and keeping \mathbf{v} and \mathbf{h}_1 fixed, displays continuous sections of the orientation space, each displayed with equal area and in the same amount of computer processing time.

The view is complete in the sense that two different data sets are not displayed in the same way. The superposition of all sections is the \mathbf{h} -pole point or pole density plot.

Instead of varying ω , it could be fixed, and either \mathbf{v} or \mathbf{h}_1 can be varied. For fixed $\omega = 0$, or $\omega = \pi/2$, respectively, and fixed \mathbf{h}_1 , varying \mathbf{v} over the whole pole sphere corresponds to exploring ‘where is \mathbf{h}_1 headed to?’. The answer is provided by the most dense clusters of orientations. As before, the sections sum to the \mathbf{h} -pole point plot and display the entire orientation space, each with equal area and in the same amount of computer time. The view is complete in the sense that two different data sets are not displayed in the same way. For every set of parameters with $\omega \in \{0, \pi/2, \pi, 3\pi/2\}$ the user can easily infer the \mathbf{h}_1 direction of every displayed orientation due to its simple relationship with respect to the direction \mathbf{v} .

Exchanging the roles of \mathbf{v} and \mathbf{h}_1 allows exploration of the data according to ‘which crystallographic direction heads to \mathbf{v} ?’. This sectioning has the same properties as the previous one.

It is not recommended to vary \mathbf{h} and keep all other parameters defining ω sections fixed. Varying \mathbf{h} has totally different

effects; the corresponding sections do not sum to pole point or pole density plots, but to a uniform distribution instead. They do not display the entire orientation space, neither in equal area nor in the same time, and the view is not complete.

A computer program allows the user to change the parameters interactively by a single mouse click or drag, and displays the parameters of the plot within the plot. This behaviour is important since it allows the user to explore the data by changing the projections and sections rapidly in a well controlled way and with minimum eye movement. The approach is driven by actively displaying specific regions of the orientation space.

When, by particular choice of $\mathbf{h}_1 = \mathbf{x}_{K_C}$ and $\mathbf{v} = \mathbf{z}_{K_S}$, ω sections are used to display ordinary γ sections, they suffer of course from the same defect as described by Helming *et al.* (1988) that similar orientations are visualized in different γ sections. This defect was actually visualized in the (100)-pole figure of a central von Mises–Fisher orientation probability density function with centre $\mathbf{g}_0 = (0,0,0)$ and halfwidth of $\pi/12$ in the case of cubic crystal symmetry. It was explained by the singularity of the representation of orientations in terms of Euler angles at $\beta = 0$ and $\beta = \pi$, respectively. If $(\alpha, \beta, \gamma) = (\tau, 0, 2\sigma - \tau)$, $2\sigma = \alpha + \gamma$, then orientations with fixed σ but varying τ will be plotted at different locations of the pole sphere, even though they represent essentially the same orientation and cannot be distinguished. Orientations with fixed τ and varying σ will be plotted at the same location, but can be distinguished. In γ sections, they can be distinguished by the angle $\omega = 2\sigma - \tau$ included by \mathbf{z}_{K_S} and $\mathbf{g}\mathbf{x}_{K_C}$ when orthogonally projected onto the tangential plane. In the case of the example of Helming *et al.* (1988), the orientations are largely concentrated around $\mathbf{g}_0 = (0,0,0)$. Therefore, the directions $\mathbf{g}\mathbf{x}_{K_C}$ are largely concentrated around \mathbf{x}_{K_S} . Therefore, the angle included by \mathbf{z}_{K_S} and $\mathbf{g}\mathbf{x}_{K_C}$ when orthogonally projected onto the tangential plane at the pole point with spherical coordinates (α, ε) with small $\varepsilon \geq 0$, is largely concentrated around α . Thus, the defect of the γ sections may now be understood as the effect of small β rotations in terms of the new interpretation of γ sections.

Thus, the same effect occurs in any \mathbf{h} -pole figure whenever the direction \mathbf{v} is chosen such that $\mathbf{v} = \mathbf{g}_0\mathbf{h}$.

Instead of introducing σ sections (Helming *et al.*, 1988; Matthies *et al.*, 1990a,b) as a remedy, we suggest here to proceed from γ to ω sections by choosing just a different specimen direction \mathbf{v} with a sufficiently large distance of $\mathbf{g}_0\mathbf{h}$. Moreover, σ sections can be interpreted as ω sections with a varying specimen direction \mathbf{v} , which must actually be chosen as $\mathbf{v} = M(-\alpha; \mathbf{r})\mathbf{z}_{K_S}$, because then it holds that

$$\omega - \alpha = \pi - \gamma - \alpha = \pi - 2\sigma.$$

6.1. Visualizing orientations with linked views

An alternative and complementary approach to visualize the information conveyed by rotation/orientation data of crystal grains in pole point plots is provided by highlighting in

dynamically linked views (Theus, 1996; Thierney, 1991; Velleman, 1997), which belongs to the realm of exploratory data analysis. The user selects an orientation in a pole point or orientation section view with a mouse click, and this orientation is instantaneously highlighted (*e.g.* by colouring in yellow) in all other opened views. ‘Brushing’ refers to transient selections of orientations made ‘on the fly’ and expunged as soon as the mouse leaves their neighbourhood.

Displaying linked pole point views and brushing over them enables the user to see where the other crystallographic axes of a grain specified by a specific direction of one crystallographic axis point to. While dynamically linked pole point views of different crystal forms provide the complete information concerning a subset of crystal grains selected by the user, section views provide information concerning a subset of the orientation space selected by the user. Brushing pole point views allows a rapid display of the orientation information for the entire data set. Pole point views are complete in the sense that two different data sets of individual crystallographic orientations differ in at least one pole point view.

It is emphasized that reasonable brushing of pole point views corresponds to a selection within a constant-area spherical cap of the pole sphere. Then brushing has the same equal-area property as sectioning of the orientation space. This property is essential for a well controlled exploratory data analysis and its easy interpretation.

Fixing the active selection displaying a special and interesting subset of orientations by assigning a colour to the currently selected points, known as ‘colouring’ in interactive statistical graphics, allows the user to view different groups and orientation relationships simultaneously.

7. Examples

The von Mises–Fisher matrix or, equivalently, the Bingham distribution for rotations represented by unit quaternions in $S^3 \subset \mathbb{R}^4$ provides a model for three different patterns of preferred crystallographic orientation: (i) bimodal axial, (ii) multimodal circular and (iii) multimodal spherical; if the distribution is rotationally symmetric, the three cases refer to a simple texture, a fibre texture, and a spherical surface texture (component), respectively (*cf.* Schaeben, 1996; Kunze & Schaeben, 2004). Individual rotation data according to the three cases have been simulated with the parameter matrix

$$F = KM \quad (33)$$

decomposed into the elliptical component K and the polar component M . In all three cases, M has been chosen to represent the identical rotation

$$M = \begin{pmatrix} 1 & 0 & 0 \\ 0 & 1 & 0 \\ 0 & 0 & 1 \end{pmatrix}.$$

To simulate rotationally symmetric distributions, the elliptical component has been chosen as follows.

(a) In case (i) of an axial simple texture,

$$K_1 = \kappa \begin{pmatrix} 1 & 0 & 0 \\ 0 & 1 & 0 \\ 0 & 0 & 1 \end{pmatrix}, \quad \kappa = 50.$$

(b) In case (ii) of a fibre texture,

$$K_2 = \kappa \begin{pmatrix} 0 & 0 & 0 \\ 0 & 0 & 0 \\ 0 & 0 & 1 \end{pmatrix}, \quad \kappa = 50.$$

(c) In case (iii) of a ring fibre texture,

$$K_3 = -\kappa \begin{pmatrix} 1 & 0 & 0 \\ 0 & 1 & 0 \\ 0 & 0 & 1 \end{pmatrix}, \quad \kappa = 50.$$

For all three cases, and triclinic crystal symmetry, first the spherical Radon transform is displayed for $\mathbf{h} = (001)^t$ and $\mathbf{h} = (111)^t$ in equal-area projection of the lower and upper hemisphere, both as pole point plot and pole density plot; then the pole point plot of the spherical Radon transform for $\mathbf{h} = (001)^t$ augmented by $\mathbf{h}_1 = (111)^t$ and $\mathbf{v} = (010)^t$ is depicted; and then the spreading of the $(001)^t$ -pole point figure into ω sections with respect to $\mathbf{h}_1 = (111)^t$ and $\mathbf{v} = (010)^t$ is exposed.

Eventually, for all three cases, and trigonal symmetry, first the crystallographic X-ray transform is displayed for $\mathbf{h} = (001)^t$ and $\mathbf{h} = (111)^t$ in equal-area projection of the lower and upper hemisphere as pole point plot; then the pole point plot of the crystallographic X-ray transform for $\mathbf{h} = (001)^t$ augmented by $\mathbf{h}_1 = (111)^t$ and $\mathbf{v} = (010)^t$ is depicted; and then the spreading of the $(001)^t$ -pole point figure into ω sections with respect to $\mathbf{h}_1 = (111)^t$ and $\mathbf{v} = (010)^t$ is exposed.

7.1. Radon transforms and ω section in the case of triclinic crystal symmetry

For the symmetrical bimodal axial case of the von Mises–Fisher distribution (simple texture), the $\mathbf{h} = (001)^t$ and the $\mathbf{h} = (111)^t$ -pole point (Figs. 3 and 5) and pole density plots (Figs. 4 and 6) show a strong circularly symmetrical maximum at $\mathbf{r} = (001)^t$ and $\mathbf{r} = 1/3^{1/2}(111)^t$, respectively. The augmented $(001)^t$ -pole point plot (Fig. 7) shows that $\mathbf{g}_i(111)^t$ displayed at $\mathbf{r}_i = \mathbf{g}_i(001)^t$ point to $1/3^{1/2}(111)^t$ with little deviation. The ω sections (Fig. 8) reveal that the distribution of the angles enclosed by the orthogonal projections of $\mathbf{g}_i\mathbf{h}_1 = \mathbf{g}_i(111)^t$ and $\mathbf{v} = (010)^t$ onto the tangential plane at $\mathbf{r}_i = \mathbf{g}_i(001)^t$ is unimodally symmetrically and strongly concentrated at $-\pi/4$.

For the symmetrical circular case of the von Mises–Fisher distribution (fibre texture), the $\mathbf{h} = (001)^t$ -pole point (Fig. 9) and the pole density (Fig. 10) plots show a strong circularly symmetrical maximum at $\mathbf{r} = (001)^t$. The $\mathbf{h} = (111)^t$ -pole point (Fig. 11) and pole density (Fig. 12) plot show a symmetrical small circle distribution with an aperture angle of 54° . The augmented $(001)^t$ -pole point plot (Fig. 13) indicates a uniform distribution of the angles enclosed by the orthogonal projections of $\mathbf{g}_i\mathbf{h}_1 = \mathbf{g}_i(111)^t$ and $\mathbf{v} = (010)^t$ onto the tangential plane at $\mathbf{r}_i = \mathbf{g}_i(001)^t$. The ω sections (Fig. 14) confirm the uniform distribution.

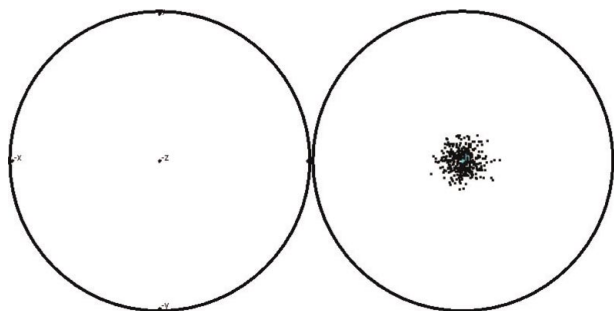


Figure 3
Pole point plot of the spherical Radon transform of the axial distribution (simple axial texture) for $\mathbf{h} = (001)^t$ in equal-area projection of the lower (left) and the upper (right) hemisphere.

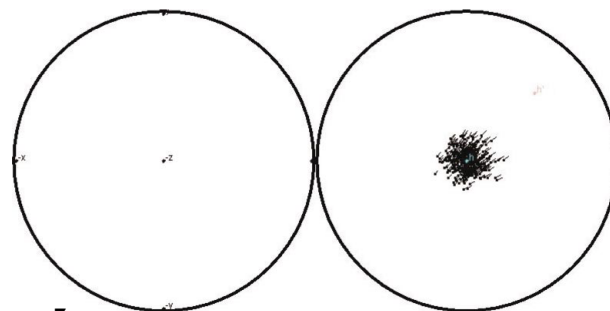


Figure 7
Augmented pole point plot of the spherical Radon transform of the axial distribution for $\mathbf{h} = (001)^t$ in equal-area projection of the lower (left) and the upper (right) hemisphere, displaying the direction of (111) at each pole point $\mathbf{h}_1 = \mathbf{g} \cdot \mathbf{h}$

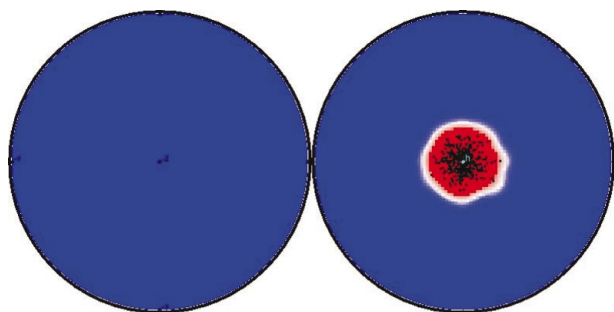


Figure 4
Pole density plot of the spherical Radon transform of the axial distribution for $\mathbf{h} = (001)^t$ in equal-area projection of the lower (left) and the upper (right) hemisphere.

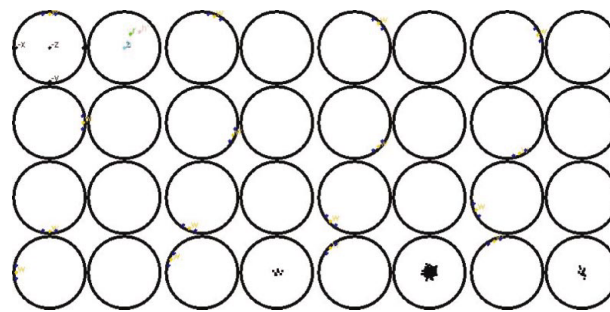


Figure 8
 ω sections of the (001)-pole point plot of the spherical Radon transform of the axial distribution with step size $\Delta\omega = 11.25$.

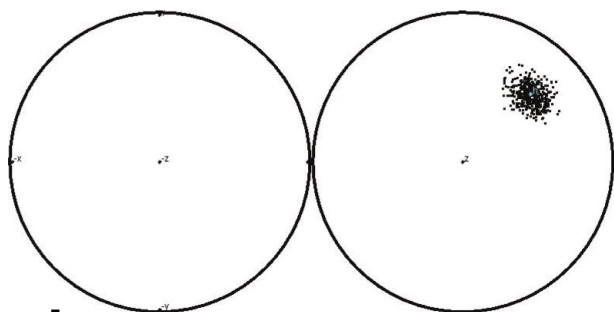


Figure 5
Pole point plot of the spherical Radon transform of the axial distribution for $\mathbf{h} = (111)^t$ in equal-area projection of the lower (left) and the upper (right) hemisphere.

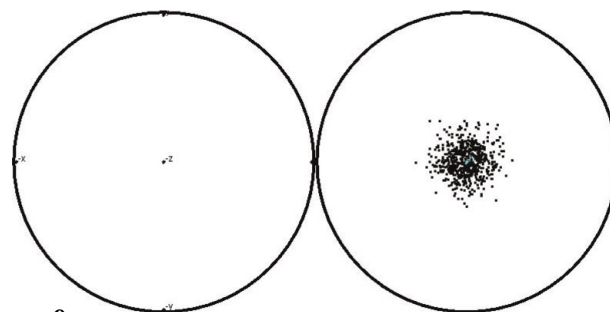


Figure 9
Pole point plot of the spherical Radon transform of the circular distribution for $\mathbf{h} = (001)^t$ in equal-area projection of the lower (left) and the upper (right) hemisphere.

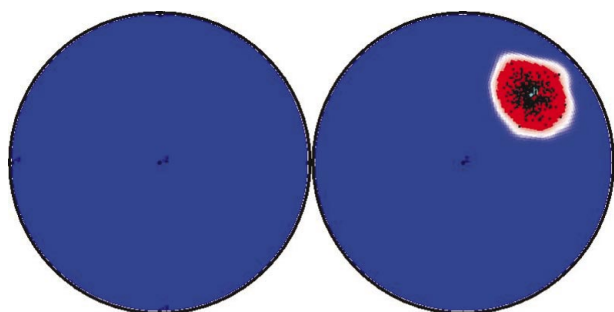


Figure 6
Pole density plot of the spherical Radon transform of the axial distribution (simple axial texture) for $\mathbf{h} = (111)^t$ in equal-area projection of the lower (left) and the upper (right) hemisphere.

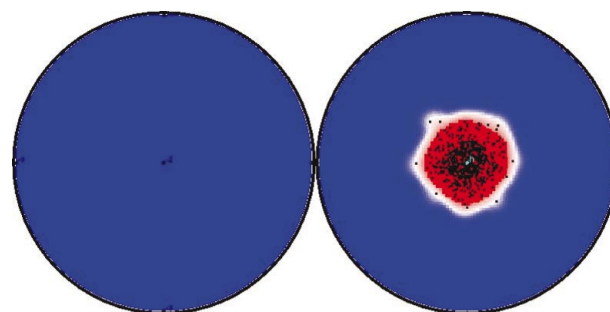


Figure 10
Pole density plot of the spherical Radon transform of the circular distribution for $\mathbf{h} = (001)^t$ in equal-area projection of the lower (left) and the upper (right) hemisphere.

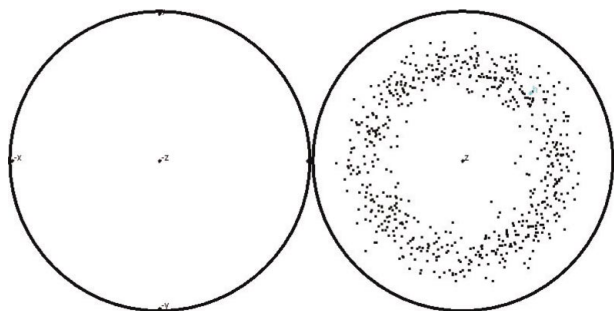


Figure 11
Pole point plot of the spherical Radon transform of the circular distribution for $\mathbf{h} = (111)^t$ in equal-area projection of the lower (left) and the upper (right) hemisphere.

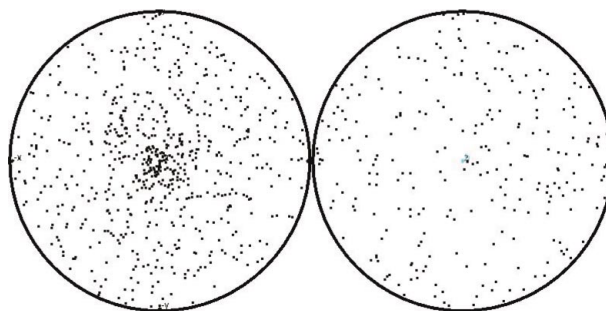


Figure 15
Pole point plot of the spherical Radon transform of the spherical distribution for $\mathbf{h} = (001)^t$ in equal-area projection of the lower (left) and the upper (right) hemisphere.

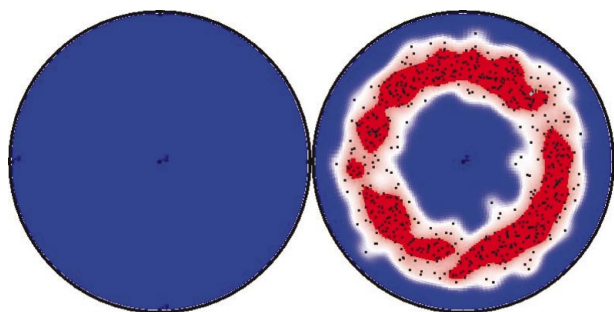


Figure 12
Pole density plot of the spherical Radon transform of the circular distribution for $\mathbf{h} = (111)^t$ in equal-area projection of the lower (left) and the upper (right) hemisphere.

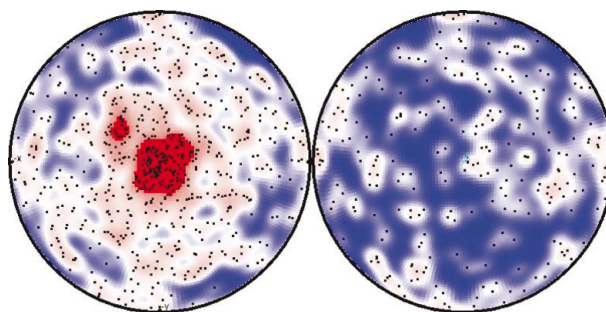


Figure 16
Pole density plot of the spherical Radon transform of the spherical distribution for $\mathbf{h} = (001)^t$ in equal-area projection of the lower (left) and the upper (right) hemisphere.

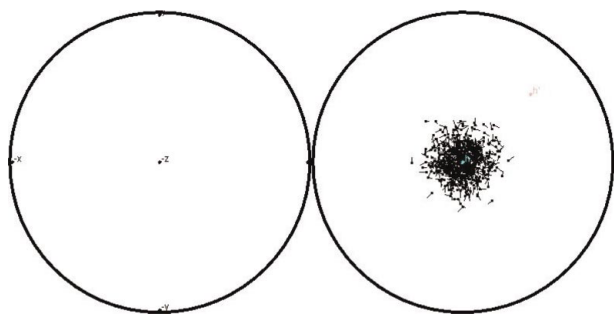


Figure 13
Augmented pole point plot of the spherical Radon transform of the circular distribution for $\mathbf{h} = (001)^t$ in equal-area projection of the lower (left) and the upper (right) hemisphere, displaying the direction of (111) at each pole point $\mathbf{h}_i = \mathbf{g}_i \mathbf{h}$.

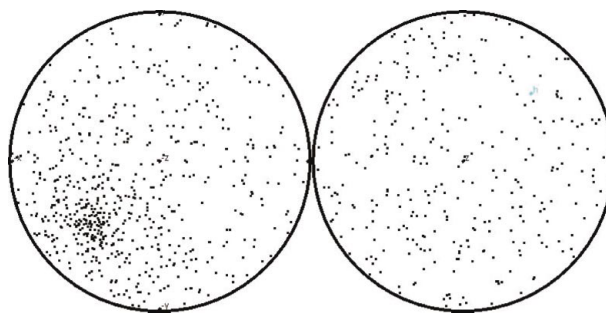


Figure 17
Pole point plot of the spherical Radon transform of the spherical distribution for $\mathbf{h} = (111)^t$ in equal-area projection of the lower (left) and the upper (right) hemisphere.

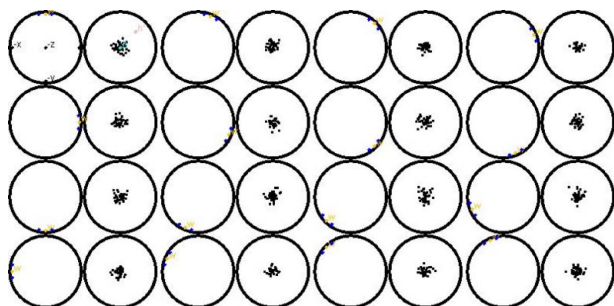


Figure 14
 ω sections of the (001) -pole point plot of the spherical Radon transform of the circular distribution with step size $\Delta\omega = 11.25$.

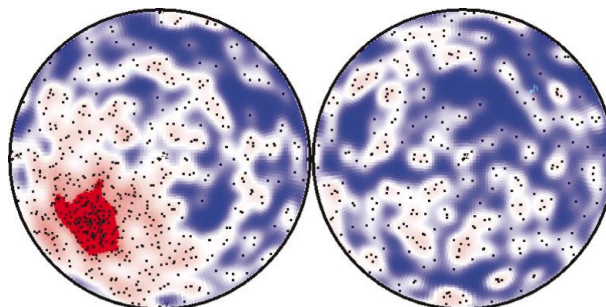


Figure 18
Pole density plot of the spherical Radon transform of the spherical distribution for $\mathbf{h} = (111)^t$ in equal-area projection of the lower (left) and the upper (right) hemisphere.

For the symmetrical spherical case of the von Mises–Fisher distribution (spherical surface texture), both the $\mathbf{h} = (001)^f$ and the $\mathbf{h} = (111)^f$ -pole point (Figs. 15 and 17) and pole density plots (Figs. 16 and 18) show a weak circularly symmetrical maximum at $\mathbf{r} = -(001)^f$ and $\mathbf{r} = -1/3^{1/2}(111)^f$, respectively. The augmented $(001)^f$ -pole point plot (Fig. 19) exposes a distinguished pattern of $\mathbf{g}_i(111)^f$ directions displayed at $\mathbf{r}_i = \mathbf{g}_i(001)^f$. The ω sections (Fig. 20) show that the distribution of the angles enclosed by the orthogonal projections of $\mathbf{g}_i\mathbf{h}_1 = \mathbf{g}_i(111)^f$ and $\mathbf{v} = (010)^f$ onto the tangential plane at $\mathbf{r}_i = \mathbf{g}_i(001)^f$ is unimodally symmetrically and weakly concentrated at $3\pi/4$.

7.2. Crystallographic X-ray transforms and ω section in the case of trigonal crystal symmetry

For the symmetrical bimodal axial case of the von Mises–Fisher distribution (simple texture) with trigonal crystal symmetry imposed, the $\mathbf{h} = (001)^f$ and the $\mathbf{h} = (111)^f$ -pole point (Figs. 21 and 22) show a strong circularly symmetrical maximum at $\mathbf{r} = \pm(001)^f$ and $\mathbf{r} = \pm 1/3^{1/2}(111)^f$ and its symmetrical equivalents, respectively. The augmented $(001)^f$ -pole point plot (Fig. 23) shows that $\mathbf{g}_i(111)^f$ and their symmetrical equivalents displayed at $\mathbf{r}_i = \mathbf{g}_i(001)^f$ point to $1/3^{1/2}(111)^f$ and their symmetrical equivalents with little deviations. The ω sections (Fig. 24) reveal that the distribution of the angles enclosed by the orthogonal projections of $\mathbf{g}_i\mathbf{h}_1 = \mathbf{g}_i(111)^f$ and $\mathbf{v} = (010)^f$ onto the tangential plane at $\mathbf{r}_i = \mathbf{g}_i(001)^f$ is symmetrically multimodal and strongly concentrated at $(2\ell - 1)\pi/6, \ell = 1, \dots, 6$.

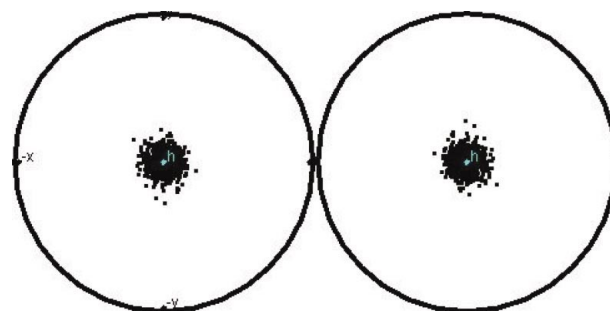


Figure 21
Pole point plot of the crystallographic X-ray transform of the axial distribution for $\mathbf{h} = (001)^f$ in equal-area projection of the lower (left) and upper (right) hemisphere.

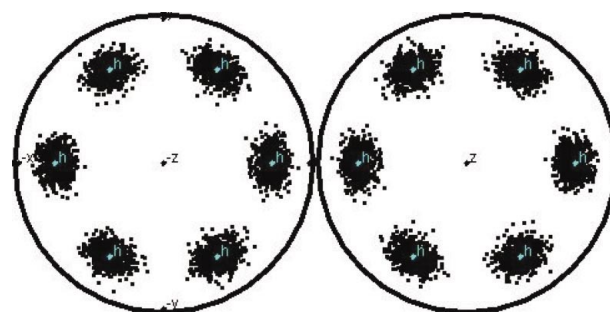


Figure 22
Pole point plot of the crystallographic X-ray transform of the axial distribution for $\mathbf{h} = (111)^f$ in equal-area projection of the lower (left) and upper (right) hemisphere.

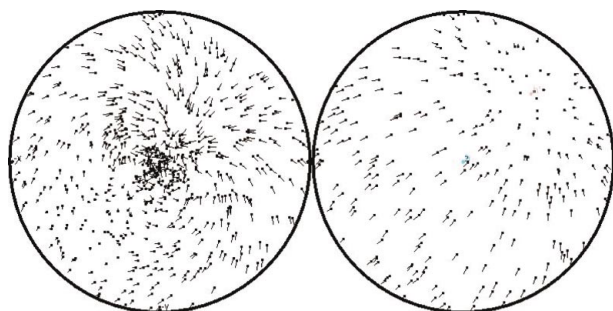


Figure 19
Augmented pole point plot of the spherical Radon transform of the spherical distribution for $\mathbf{h} = (001)^f$ in equal-area projection of the lower (left) and the upper (right) hemisphere, displaying the direction of $\mathbf{g}_i\mathbf{h}_1 = \mathbf{g}_i(111)^f$ at each pole point $\mathbf{r}_i = \mathbf{g}_i\mathbf{h}$.

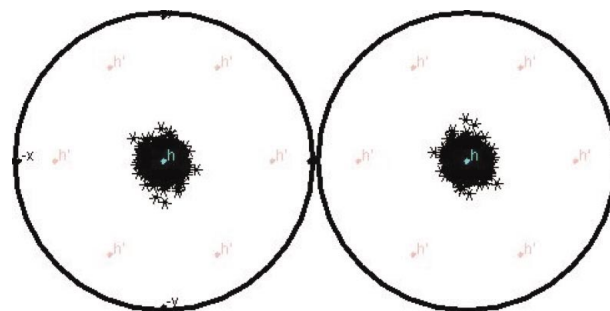


Figure 23
Augmented pole point plot of the crystallographic X-ray transform of the axial distribution for $\mathbf{h} = (001)^f$ in equal-area projection of the lower (left) and the upper (right) hemisphere, displaying the direction of $\mathbf{g}_i\mathbf{h}_1 = \mathbf{g}_i(111)^f$ and its symmetry equivalents at each pole point $\mathbf{r}_i = \mathbf{g}_i\mathbf{h}$.

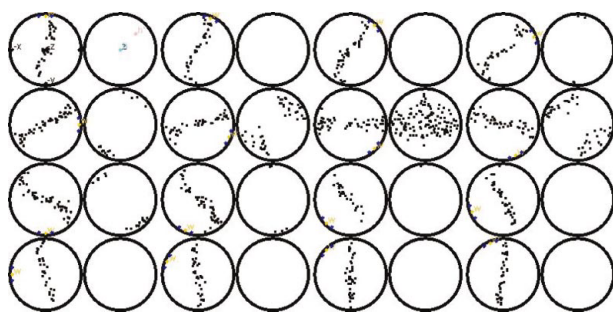


Figure 20
 ω sections of the (001) -pole point plot of the spherical Radon transform of the spherical distribution with respect to $\mathbf{h}_1 = (111)^f$ and $\mathbf{v} = (010)^f$ with step size $\Delta\omega = 11.25$.

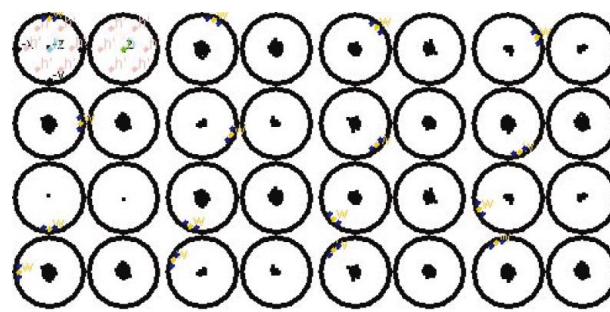


Figure 24
 ω sections of the (001) -pole point plot of the crystallographic X-ray transform of the axial distribution with respect to $\mathbf{h}_1 = (111)^f$ and $\mathbf{v} = (010)^f$ with step size $\Delta\omega = 11.25$.

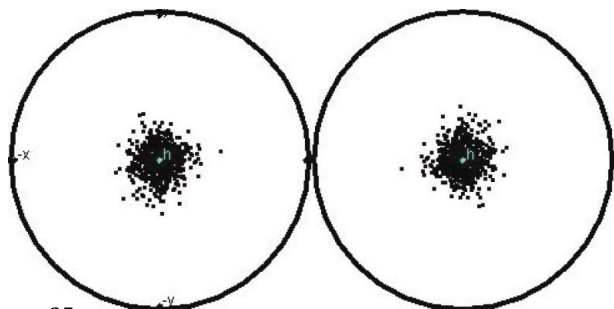


Figure 25
Pole point plot of the crystallographic X-ray transform of the circular distribution for $\mathbf{h} = (001)'$ in equal-area projection of the lower (left) and the upper (right) hemisphere.

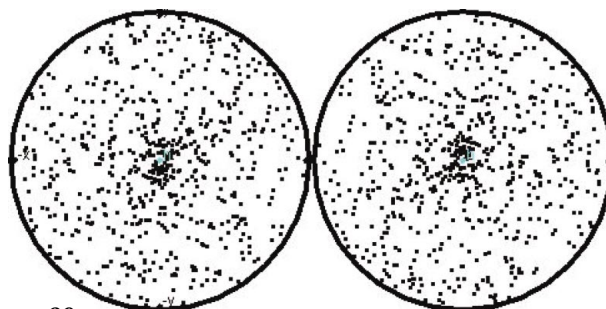


Figure 29
Pole point plot of the crystallographic X-ray transform of the spherical distribution for $\mathbf{h} = (001)'$ in equal-area projection of the lower (left) and the upper (right) hemisphere.

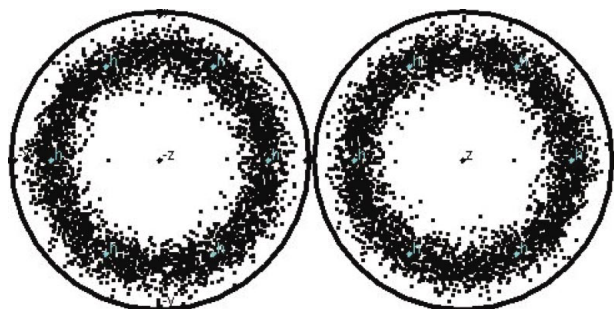


Figure 26
Pole point plot of the crystallographic X-ray transform of the circular distribution for $\mathbf{h} = (111)'$ in equal-area projection of the lower (left) and the upper (right) hemisphere.

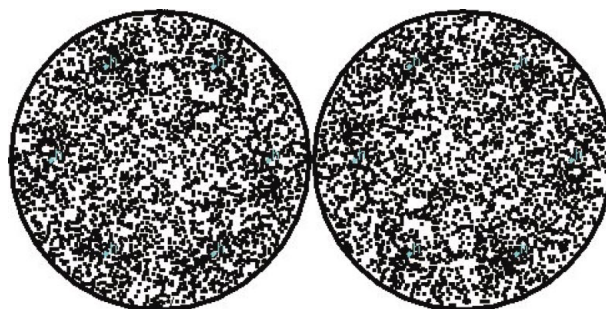


Figure 30
Pole point plot of the crystallographic X-ray transform of the spherical distribution for $\mathbf{h} = (111)'$ in equal-area projection of the lower (left) and the upper (right) hemisphere.

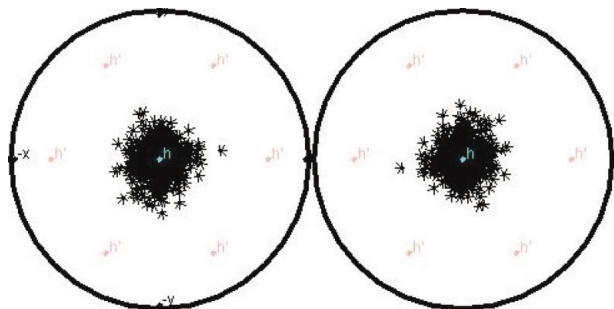


Figure 27
Augmented pole point plot of the crystallographic X-ray transform of the circular distribution for $\mathbf{h} = (001)'$ in equal-area projection of the lower (left) and the upper (right) hemisphere, displaying the direction of \mathbf{g} , $\mathbf{h}_1 = \mathbf{g}_i(111)'$ and its symmetry equivalents at each pole point $\mathbf{r}_i = \mathbf{g} \cdot \mathbf{h}$.

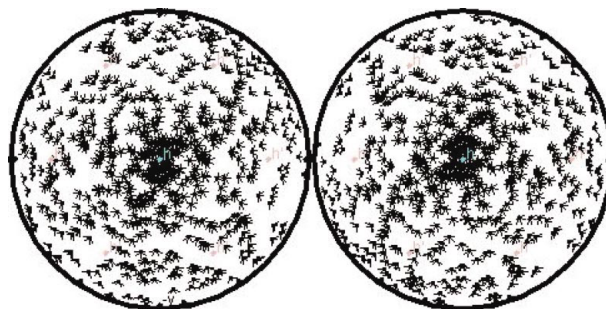


Figure 31
Augmented pole point plot of the crystallographic X-ray transform of the spherical distribution for $\mathbf{h} = (001)'$ in equal-area projection of the lower (left) and the upper (right) hemisphere, displaying the direction of \mathbf{g} , $\mathbf{h}_1 = \mathbf{g}_i(111)'$ and its symmetry equivalents at each pole point $\mathbf{r}_i = \mathbf{g} \cdot \mathbf{h}$.

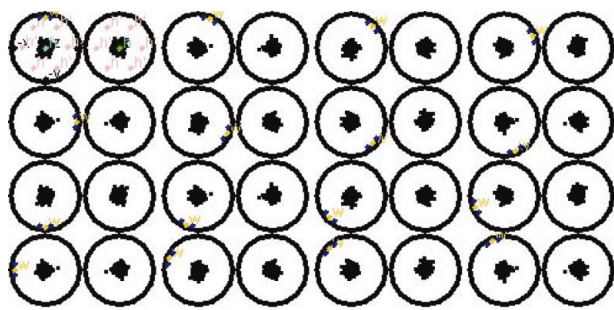


Figure 28
 ω sections of the (001)-pole point plot of the crystallographic X-ray transform of the circular distribution with respect to $\mathbf{h}_1 = (111)'$ and $\mathbf{v} = (010)'$ with step size $\Delta\omega = 11.25$.



Figure 32
 ω sections of the (001)-pole point plot of the crystallographic X-ray transform of the spherical distribution with respect to $\mathbf{h}_1 = (111)'$ and $\mathbf{v} = (010)'$ with step size $\Delta\omega = 11.25$.

For the symmetrical circular case of the von Mises–Fisher distribution (fibre texture), the $\mathbf{h} = (001)^f$ -pole point plot (Fig. 25) shows a strong circularly symmetrical maximum at $\mathbf{r} = (001)^f$. The $\mathbf{h} = (111)^f$ -pole point plot (Fig. 26) shows a symmetrical small circle distribution with an aperture angle of 54° . The augmented $(001)^f$ -pole point plot (Fig. 27) indicates a uniform distribution of the angles enclosed by the orthogonal projections of \mathbf{g}_i , $\mathbf{h}_1 = \mathbf{g}_i(111)^f$ and $\mathbf{v} = (010)^f$ onto the tangential plane at $\mathbf{r}_i = \mathbf{g}_i(001)^f$. The ω sections (Fig. 28) confirm the uniform distribution.

For the symmetrical spherical case of the von Mises–Fisher distribution (spherical surface texture), the $\mathbf{h} = (001)^f$ and the $\mathbf{h} = (111)^f$ -pole point plot (Figs. 29 and 30) show a weak circularly symmetrical maximum at $\mathbf{r} = -(001)^f$ and $\mathbf{r} = -1/3^{1/2}(111)^f$ and its symmetrical equivalents, respectively. The augmented $(001)^f$ -pole point plot (Fig. 31) exposes a distinguished pattern of $\mathbf{g}_i(111)^f$ directions displayed at $\mathbf{r}_i = \mathbf{g}_i(001)^f$. The ω sections (Fig. 32) show that the distribution of the angles enclosed by the orthogonal projections of \mathbf{g}_i , $\mathbf{h}_1 = \mathbf{g}_i(111)^f$ and $\mathbf{v} = (010)^f$ onto the tangential plane at $\mathbf{r}_i = \mathbf{g}_i(001)^f$ is uniform.

8. Conclusions

Any information concerning the location of contributing grains or orientational relationships of neighbouring grains would require different data and different experimental techniques than X-ray or neutron diffraction, and eventually methods of orientation mapping. The display of orientation and pole probability density functions conveys only summary information about the texture. Therefore, an orientation probability density function should be displayed in the most sensible possible way, providing the best possible insight by exhibiting simultaneous orientational relationships of two different crystal axes with two different specimen directions in ω sections such that their superposition yields a user-specified pole probability density function. Most instructively, with an augmented pole point plot or the corresponding ω sections, respectively, the bimodal axial and the multimodal spherical von Mises–Fisher distribution can be distinguished with a single plot.

The authors would like to thank Heiko Kost, Anidesk Digitalvisualization, Webenheim, Germany, for providing the Figs. 1 and 2, and an animated three-dimensional visualization which proved a valuable tool in teaching.

References

- Altmann, S. L. (1986). *Rotations, Quaternions and Double Groups*. Oxford University Press.
- Bukharova, T. I. (1996). *Texture Microstruct.* **25**, 205–210.
- Bunge, H. J. (1969). *Mathematische Methoden der Texturanalyse*. Berlin: Akademie Verlag.
- Bunge, H. J. (1982). *Texture Analysis in Materials Science*. London: Butterworth.
- Cerejeiras, P., Schaeben, H. & Sommen, F. (2002). *Math. Methods Appl. Sci.* **25**, 1493–1507.
- Funk, P. (1913). *Math. Ann.* **74**, 278–300.
- Funk, P. (1916). *Math. Ann.* **77**, 129–135.
- Helgason, S. (1959). *Acta Math.* **102**, 239–299.
- Helming, K., Matthies, S. & Vinel, G. W. (1988). *Proceedings of the 8th International Conference on Textures of Materials 1987*, pp. 55–60. Littleton: American Institute of Mining, Metallurgical and Petroleum Engineers.
- Kocks, U. F., Tomé, C. N. & Wenk, H. R. (1999). *Texture and Anisotropy*. Cambridge University Press.
- Kuipers, J. B. (1999). *Quaternions and Rotation Sequences – A Primer with Applications to Orbits, Aerospace and Virtual Reality*. Princeton University Press.
- Kunze, K. (1991). PhD thesis, RWTH Aachen, Germany.
- Kunze, K. & Schaeben, H. (2004). *Math. Geol.* In the press.
- Matthies, S., Helming, K. & Kunze, K. (1990a). *Phys. Status Solidi B*, **157**, 71–83.
- Matthies, S., Helming, K. & Kunze, K. (1990b). *Phys. Status Solidi B*, **157**, 489–507.
- Matthies, S., Vinel, G. W. & Helming, K. (1987). *Standard Distributions in Texture Analysis*, Vol. I. Berlin: Akademie Verlag.
- Meister, L. (1997). Habilitationsschrift, TU Freiberg, Germany.
- Meister, L. & Schaeben, H. (2004). *Math. Methods Appl. Sci.* In the press.
- Radon, J. (1917). *Berichte über die Verhandlungen der Königlich Sächsischen Gesellschaft der Wissenschaften zu Leipzig, Math.-Phys. Klasse* 69, 262–277.
- Schaeben, H. (1996). *J. Appl. Cryst.* **29**, 516–525.
- Schaeben, H. & van den Boogaart, K. G. (2002). *Proceedings of the 8th Annual Conference of the International Association for Mathematical Geology*, pp. 443–448. Berlin: Terra Nostra.
- Schaeben, H. & van den Boogaart, K. G. (2003). *Proceedings of the 51th Denver X-ray Conference*. Newtown Square: International Centre for Diffraction Data. In the press.
- Schaeben, H., Spröβig, W. & van den Boogaart, K. G. (2001). *Proceedings of the NATO Advanced Research Workshop Prague*, pp. 283–291. Dordrecht: Kluwer.
- Theus, M. (1996). *Theorie und Anwendung Interaktiver Statistischer Graphik*. Augsburg: Wißner.
- Thierney, L. (1991). *LISP-STAT: An Object-Oriented Environment for Statistical Computing and Dynamic Graphics*. New York: Wiley.
- Velleman, P. F. (1997). *Data Desk Handbook, Statistics Guide*, 6th ed., revised and extended. Ithaca: Data Description.
- Wenk, H. R. & Kocks, U. F. (1987). *Met. Trans. A*, **18**, 1083–1092.